Demography of sunspots: aging, and death by turbulent erosion?

Matthew D. Schwartz*
Department of Physics, Harvard University

Cecilia Garraffo
AstroAI, Center for Astrophysics | Harvard & Smithsonian

Abstract

Sunspots are dark patches on the Sun's surface where concentrated magnetic fields choke off the heat rising from below; they emerge in groups, grow, and dissolve over days to weeks. Since the Sun rotates, every group leaves view within about nine days, so quantifying their lifetimes is difficult, and proposed laws disagree by a factor of four. We determine the lifetime distributions by applying the survival analysis of biodemography, summing over every admissible threading of the registry's broken life histories. We find that individual sunspot groups seem to age. At fixed size and fixed hardiness, a group's risk of dying rises about twenty percent per day in our baseline model. Aging also speeds up in a window that opens near each cycle maximum, as the polar field reverses, by an amount that varies from cycle to cycle and fades from maximum over about two years, tracking the cycle's own decline. All published decay laws, cast as death-risk laws, fail against these observations. To find a physical mechanism, we cast and adjudicated six published mechanisms, seventeen aging mechanisms of our own, and roughly fifty candidate modulation mechanisms and carriers, none of which the data establish. The one not eliminated, threshold collapse at a deep anchor, is a physical hypothesis consistent with the measured law: a group would die when turbulent erosion thins its subsurface root past a breaking point. That premise yields the rising-risk law at a rate the convection zone's eddy turnover can supply. More broadly, a mechanism for how sunspot groups die turns their lifetimes into a probe of the Sun beneath the surface. The same demographic approach we used to understand sunspots can also be used to study a variety of solar phenomena, from the nests in which spot groups emerge, to plage, filaments and pores.

1 Introduction

What kills a sunspot group remains an open question. A sunspot is a place where the Sun's magnetic field has gathered into a bundle strong enough to choke off the convection beneath it, so the patch runs cooler and appears dark. Spots emerge in groups, and a group is born, grows, decays, and disappears over days to weeks. Over the past century solar physicists have attributed a group's death to erosion by the surrounding convection (Simon and Leighton, 1964; Petrovay and Moreno-Insertis, 1997; Litvinenko and Wheatland, 2015), to decay at a rate set by current size (Gnevyshev, 1938; Waldmeier, 1955), and to clocks wound at birth (Bradshaw and Hartigan,

*Work done with Anthropic, but results and views are not endorsed by Anthropic.

2014). In the Gnevyshev–Waldmeier tradition a spot's area shrinks at a constant rate, implying the lifetime–area law $\tau = \alpha A_{\max}$ (Gnevyshev, 1938; Waldmeier, 1955). Disk-based estimates give $\alpha \approx 0.1$ d/MSH (days per millionth of the solar hemisphere) (Gnevyshev, 1938; Waldmeier, 1955; Petrovay and van Driel-Gesztelyi, 1997), long-lived recurrent groups give 0.3–0.8 d/MSH (Muraközy, 2024), and far-side helioseismology gives $\alpha = 0.025\,(+0.055/-0.016)$ d/MSH (Chaplin et al., 2026), whose central value is a quarter of the disk-based one, though its upper uncertainty reaches most of the way to it.

The standard accounts (Gnevyshev, 1938; Waldmeier, 1955; Simon and Leighton, 1964; Petrovay and Moreno-Insertis, 1997; Litvinenko and Wheatland, 2015) set a group's fate by its present state; cast as death-risk laws they are memoryless, and at fixed present state, age adds nothing. The question of this paper is whether that picture survives the registry and, when it does not, what a rising risk at fixed visible state forces the physics of spot death to contain. Why a group dies matters beyond the Sun's bookkeeping: the answer decides between erosion at the surface, which keeps no memory of age, and a root that weakens beneath it, which does (Section 4), and the Sun's individually followed groups are the only population that can calibrate the lifetimes of the unresolved dark features through which spots are seen on other stars (Giles et al., 2017; Namekata et al., 2019; Basri et al., 2022), lifetimes that set the timescale of the activity signals limiting the search for small planets.

For the most basic question of demography, whether an individual's death rate rises as it grows older, the Greenwich–USAF registry of sunspot groups (Hathaway, 2024) is ideal. Yet the question has gone unanswered because the Sun's rotation carries a group over the west limb after at most about nine days in view (Section 2.2). A group that survives the far-side passage returns over the east limb as a recurrent group, where observers almost always log it as a new group (Henwood et al., 2010; Muraközy, 2024). Each of the three camps that estimate sunspot lifetimes works in a different censoring regime: limb truncation biases the disk-based estimates short, the recurrent-group work patches the far side by assumption, and the helioseismic fit ties lifetime to peak area through a single law, whose preferred α does not move when scatter about the law is allowed. We found no published survival analysis of sunspot or starspot lifetimes, and no hazard models, Turnbull estimators (Turnbull, 1976), or frailty fits applied to sunspot groups or to any starspot analog.[1]

We analyze the registry with survival analysis, the statistics of waiting times to an event when many of the times are observed only in part (Kaplan and Meier, 1958; Cox, 1972; Aalen and Gjessing, 2001). A group contributes its days at risk and its day of death if it died in view. A group that rotates out of sight alive counts toward the death rates up to its last day, so every censored history stays in the likelihood. We thread the record into an interval-censored panel of 42,578 life-history segments and treat far-side returns in two ways, censoring at the west limb or matching returns under the solar rotation law (Section 2.2). This paper is a measurement of catalogs; no claim that any published lifetime study is wrong.

We measure two things: the population's life table, the probability that a group still alive at a given age dies within the next day, and the individual risk, a single group's own death rate (or hazard) as a function of its age at fixed current size (Sections 3.1 and 3.2). Since each group dies only once, we infer the individual risk from the whole population with a model that lets groups differ in an unobserved hardiness, the frailty. Frail groups die first, the survivors at late ages are

[1] The closest use of survival analysis on any solar object is a Kaplan–Meier mean lifetime for chromospheric swirls (Dakanalis et al., 2022). Astronomy's survival-analysis tradition (Feigelson and Nelson, 1985) treats censored fluxes and upper limits; tracked-object lifetimes lie outside it.

the hardy minority, and the mixture's hazard falls while every individual's rises. We find that at fixed current area and fixed frailty the daily risk of dying rises about twenty percent per day under the preregistered model, +0.184 per day in log hazard. The rise and its positive sign hold across the area forms, frailty shapes, and censoring conventions fitted, though the size of the slope is conditional on them (Section 3.2). We then cast the published decay laws as death-risk laws under three bridge assumptions of our own and test them against this measurement (Section 2.4, Table A3). We repeat the population measurement on two independent catalogs (Section 3.3), bound the slope that false deaths could produce (Section 3.4), and ask whether the aging rate varies over the solar cycle (Section 3.5). Finally, we search the published mechanisms and candidates of our own for a physical model that the measurements admit, and develop its physical picture (Section 4).

2 Methods

2.1 Data

The Royal Greenwich Observatory photoheliographic program logged the sunspot groups visible on the disk daily from 1874 May 9 to 1976, and the USAF/NOAA network has continued the log since 1977 under its own instruments and reduction practice (Hathaway, 2024). Each line records one group on one day, its position and its corrected whole-spot area in MSH, the size we use throughout. The log holds 151 yearly files through 2024 December 31, 46,465 observing days, and 256,205 daily group records (Hathaway, 2024). We drop 712 records that carry a blank group number or an unusable central-meridian distance (unparseable or outside $\pm 90.5^\circ$), and collapse 2,201 duplicate group-days that multi-station USAF reporting produces, keeping the report with the largest corrected area, the most complete observation of that day. Figure 1 shows sample histories, the days in view, and the disk-transit geometry.

To place each death in the solar cycle, we read the cycle's phase from three long public records. The smoothed sunspot number traces the eleven-year rise and decline of spot production (SILSO World Data Center, 2026; Clette et al., 2014; Clette and Lefèvre, 2016). The polar magnetic fields, measured at the Wilcox Solar Observatory (Wilcox Solar Observatory, 2026; Scherrer et al., 1977), change sign near each cycle's maximum, at a different time in each hemisphere. That sign change is the polar-field reversal. Per-hemisphere reversal epochs are tabulated for every cycle since the mid-1950s (Makarov and Sivaraman, 1986; Pishkalo, 2019), including multiple crossings: the northern polar cap's field crossed zero three times in each of cycles 19, 20 and 24. For each cycle we take the epoch of completed reversal to be the mean of the two hemispheres' final sign changes (Makarov and Sivaraman, 1986; Pishkalo, 2019), read from the Wilcox record for cycle 25. These epochs date the reversal window fitted in Section 3.5.

To test whether the life table is a property of the sunspot groups or of the registry's observing practice, we rerun the population-hazard measurement on two independent catalogs, the Debrecen Photoheliographic Data (DPD, 1974–2018; Baranyi et al., 2016) (the registry's designated successor) and the SHARP catalog of HMI active-region patches (2010–2024; Bobra et al., 2014) (Table 1). Under the registry's rules we keep 106,517 Debrecen records in 21,734 segments, with a matching ambiguity of 14.4%. On a third catalog, from the Kislovodsk station (Kislovodsk Mountain Astronomical Station, Pulkovo Observatory, 2026; Tlatov et al., 2014), with its own reduction and digitization, we re-measure the amplitude of the aging-rate enhancement in the reversal windows of cycles 23 and 24 (Sections 3.5 and 4.1).

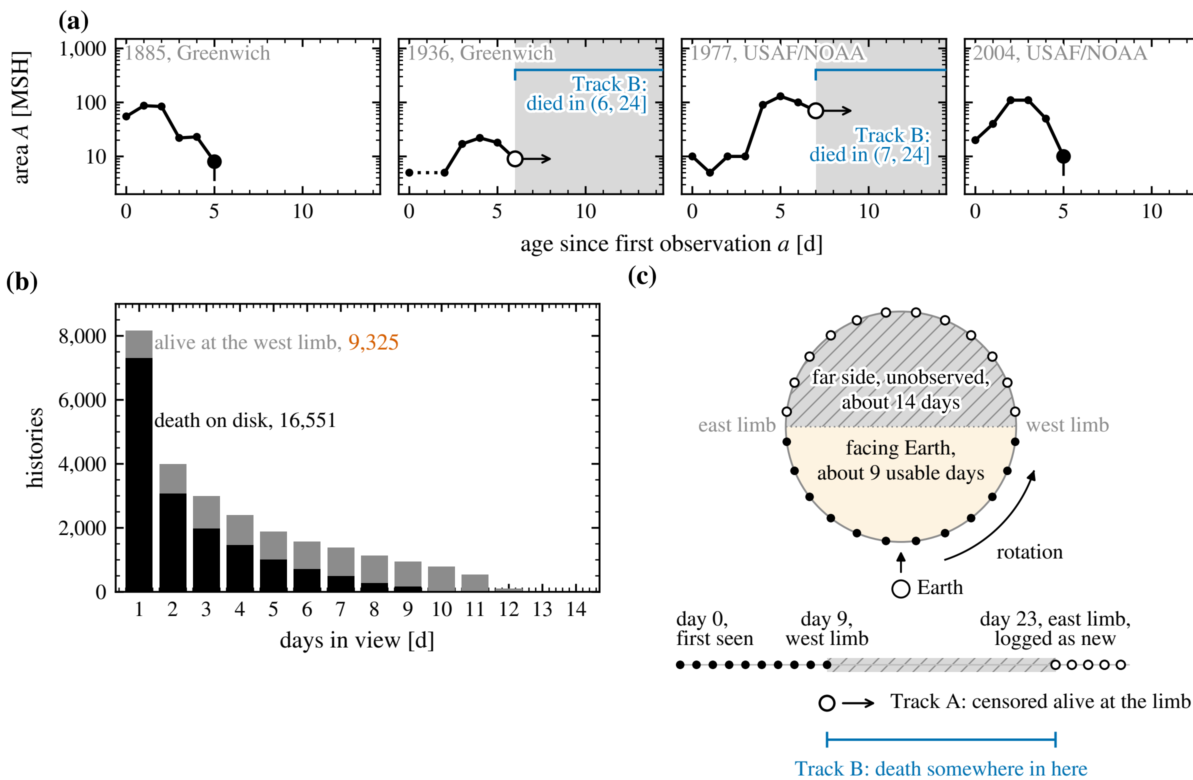

Figure 1: A sunspot group's recorded life ends either in a death seen on the disk or, alive, at the west limb: four daily area histories from the Greenwich–USAF registry, one of each ending in each era, a death on disk (1885, Greenwich; 2004, USAF/NOAA) and a limb exit that Track B codes as a far-side death (1936, Greenwich, with a one-day gap in its record; 1977, USAF/NOAA) (a); days in view of all 25,883 birth-observed histories under Track A, 16,551 ending in a recorded death and 9,325 reaching the limb alive (b); and, seen from above the Sun's pole, the rotation that carries a group across the Earth-facing half, hides it on the far side, and returns it at the east limb as a new entry in the registry, drawn without data (c). A filled last point marks a death on disk; an open point with an arrow, a history right-censored at the limb; a dotted bridge, a day missing from the group's record; a blue bracket, the far-side death interval the same group carries under Track B (Section 2.2). In (c) filled dots are days the registry records and open dots days hidden or logged as new.

2.2 Censoring conventions and threading

A group can be recorded only while it is on the Earth-facing disk, so its days on the far side, and any death there, are absent from the registry. The Sun's rotation carries every spot group around in about 27 days as seen from Earth, the synodic period at sunspot latitudes. Half of each circuit, roughly 13.6 days, is spent on the far side, and foreshortening near the limbs degrades the near-side record, so a group is measurable for at most about nine days per transit. A group is on record from its first day only if it emerged on the Earth-facing side: half of all emergences are on the far side, and those groups reach the registry only if they live to the east limb. In 150 years the compilers

catalog or series	span	records	segments or histories fitted	deaths	role in the paper
Greenwich–USAF registry	1874–2024	256,205 daily group records	42,578 segments; 25,883 birth-observed histories	16,551 on disk	Every primary fit (Sections 3.1 to 4.1)
Debrecen Photoheliographic Data	1974–2018	106,517	21,734 segments		Population-hazard replication (Section 3.3); death-versus-loss overlap control (Section 3.4)
SHARP active-region patches	2010–2024	46,823	7,206 patches		Population-hazard replication and magnetogram-era analysis (Section 3.3)
Kislovodsk station catalog					Window amplitudes of cycles 23 and 24 (Sections 3.5 and 4.1)
Sunspot number, polar field, and reversal epochs					Cycle phase and window opening (Section 3.5)

Table 1: The catalogs and series used in the paper, with the record counts the fits rest on. Deaths are counted only for the registry's birth-observed histories. On the two replication catalogs we fit the ladder of five population-hazard shapes of Section 2.4 and refit the age term on each catalog's own records (Section 3.3).

have only twice recorded a returning group as the same group seen before (for recurrent-group lifetimes see Henwood et al., 2010; Muraközy, 2024). Recurrent groups rotate at the rate Newton and Nunn measured from the Greenwich record, $\omega(\varphi) = 13.382 - 2.69 \sin^2 \varphi$ degrees per day at latitude φ (Newton and Nunn, 1951). In the language of survival analysis a complete disk transit is right-censored (the record ends with the group alive) and a far-side crossing is interval-censored (a death, if it occurred, lies inside an unobserved interval of dates). Published lifetime studies handle the far side by restriction or by assumption: Forgács-Dajka et al. (2021) keep only groups whose full history is observed on the disk, and Muraközy (2024) patches each far-side passage with an assumed 12 ± 6 days per transit.

We thread the registry under a 14-day gap rule: a gap of more than 14 days between records of one group number starts a new segment, because one far-side passage at the recurrent-group rotation rate lasts about 13.6 days, so two records further apart cannot belong to one uninterrupted stay in view. The rule yields 42,578 life-history segments. Of these, 25,883 emerged in view and are birth-observed, on record from their first day. A group first recorded 60 degrees or more east of the central meridian rotated into view at an unknown age, so we leave it out of the primary fits. Of the birth-observed histories, 16,551 end in a death observed on disk. For the rest, whose death is not observed, Track A, the conservative limb-censored convention, right-censors every segment at its last observation before the west limb. We count a last observation 60 degrees or more west of the central meridian as an exit at the limb, because disappearances at 60 to 70 degrees are near-limb detection failures; 9,325 of the birth-observed histories are right-censored at the limb and 7 at catalog seams. Track B, the rotation-matched convention, matches east-limb reappearances to west-limb exits under the Newton and Nunn (1951) rotation law for recurrent groups, and joins matched pairs into multi-transit lives. It codes an unmatched exit as a far-side death inside the return interval that the rotation law predicts, widened by two days to allow for detection failures near the limb, and right-censors an ambiguous exit.

Track B's coding of an unmatched exit as a far-side death assumes that a survivor would have reappeared and been matched. Tested against the HMI far-side seismic maps (2010–2024) under a rule and an outcome table fixed before any map was read, that assumption finds suggestive but not confirmatory support: the matching's predicted survivals are detected more often than its predicted non-survivals, although the maps see a group's magnetic region whether or not its spots survive (Appendix A). Track B's joins remain untested pair by pair (Section 5), which is why Track A was the primary convention from the design stage and of Track B we require only that the coefficient deciding each test keep its sign (Section 2.4). GONG far-side maps for 2006 to 2010 were not available at the time of writing.

Track B uses the hard kinematic windows of our pilot analysis, which keep or discard each exit-reappearance pairing outright on fixed tolerances of return time and latitude; they admit 12,373 candidate pairs and accept 3,985 unambiguous joins. They leave 8,508 of the 42,578 segments ambiguous (19.98 percent), or 4,048 (9.51 percent) counting only segments with two or more admissible partners (Appendix A). Where exits and reappearances admit more than one pairing, we also fit with the far-side matching marginalized ("matches averaged" in the figures): the likelihood sums over every admissible assignment rather than choosing one (Appendix A).

2.3 Survival analysis and frailty

Aging, in the demographer's sense, means a death rate that rises with age at fixed present state; in the models below it is the age term at fixed area and frailty.

We build the life table of sunspot groups with Turnbull's estimator (Turnbull, 1976), which gives the maximum-likelihood survival curve, of whatever shape, from one bracket per individual, alive at L_i and dead by R_i, and reduces to the Kaplan–Meier estimate when every death is observed. We run the estimator on those brackets under both tracks and read the daily hazard off the fitted curve, with 95% percentile intervals from 1,000 bootstrap replicates that resample whole histories, enough for each 2.5 percent tail to rest on 25 replicates (Efron and Tibshirani, 1993).

Vaupel et al. (1979) introduced frailty, a fixed per-individual multiplier on the hazard that stands in for unobserved hardiness, to explain mortality plateaus, population death rates that stop rising at late ages. The mortality-plateau debates of the 1990s, over medfly (Mediterranean fruit fly) cohorts and the oldest humans, settled that a flattening population death rate is consistent with individuals that keep aging (Carey et al., 1992; Vaupel et al., 1998; Steinsaltz and Wachter, 2006; Wrigley-Field, 2014). Separating selection on frailty from genuine flattening requires conditioning on an observable that carries the heterogeneity. We rank competing hazard families throughout by the Akaike information criterion (AIC), goodness of fit penalized by parameter count (Akaike, 1974), with the decisive difference fixed in Section 2.4.

2.4 Hazard models, bridge assumptions, and decision rules

We fit five hazard shapes to the life table by exact interval-censored maximum likelihood. Four are standard: constant (exponential lifetimes), Gompertz (Gompertz, 1825) (an exponentially rising hazard, the classical law of wear-out), Weibull (Weibull, 1951), and inverse-Gaussian (lifetimes as first-passage times of a diffusion, Aalen and Gjessing, 2001; Lee and Whitmore, 2006). The fifth is gamma-Gompertz, the standard biodemographic model of a mortality plateau (Vaupel et al., 1979). A group of frailty z then has the hazard

$$h_i(a) = z\, h_0\, e^{Ba}, \tag{1}$$

where h_0 is the baseline hazard level, B the age slope, and z a frailty gamma-distributed across groups with mean 1 and variance σ^2. The population hazard, averaged over the survivors at each age, tends at late ages to the plateau B/σ^2. Between them the five shapes cover the three behaviors the comparison has to separate: a hazard flat in age, one rising with age, and one decelerating. An AIC difference of 10, fixed before any fit, is decisive, the conventional threshold beyond which the weaker model retains essentially no support (Burnham and Anderson, 2002).

To separate individual aging from the selection of hardy survivors, we fit discrete-time daily-hazard models to the 25,883 birth-observed histories with their daily area paths attached, 95,468 group-days in all. We fit them under Track A, because that convention assumes nothing about the far side and imputes no area across it. These fits condition the hazard on the recorded area path day by day, treating it as a time-varying covariate rather than modeling it (Appendix B). The hazard is held constant within each day of age, so a group alive at age a dies before age $a + 1$ with probability $q_a = 1 - e^{-h_i(a)}$. The life table of Section 3.1 reports the population's per-day death probability of this kind, the discrete-time or daily death hazard, and the age slopes B are slopes of $\ln h$. The hazard depends on current area A (in MSH, through $\log(A + 1)$), on age a, and on a gamma-distributed frailty z fixed for each group. In one control we add the group's position on the disk, as $1 - \cos b \cos \lambda$ for heliographic latitude b and central-meridian distance λ, and its product with age (Section 3.2). The full model, our baseline, is

$$h_i(a) = z\, \exp\bigl[\beta_0 + \beta_1 \log(A + 1) + B\, a\bigr]. \tag{2}$$

The published decay laws (Gnevyshev, 1938; Waldmeier, 1955; Simon and Leighton, 1964; Petrovay and Moreno-Insertis, 1997; Litvinenko and Wheatland, 2015) describe how a spot's area shrinks: each is an equation for dA/dt, or a lifetime rule, in terms of the group's current state and fixed constants. The exception is the moving-boundary solution of Litvinenko and Wheatland (2015), which also carries an explicit time factor; we cast it both in its constant-speed limit and in full (Appendix C.2). None of them states a death rate, so to test them against the registry's deaths we convert each law into a hazard $h(a, A \mid \text{history})$, which we call its casting, using three assumptions that we fixed in the preregistration and applied to every law alike. (i) The published law gives the mean daily drift of the area; random variation enters as a constant multiplier per group and as day-to-day fluctuations, and the group dies when its area first falls below the catalog threshold. The scatter about the expected course therefore fixes the day of death, and a deterministic area law becomes a death rate. The fluctuations are treated as independent from day to day. Petrovay et al. (1999) measured them to be correlated over about three days, and a memoryless population with decay rates so correlated, at the measured amplitude, yields no age term that the criterion of Section 3.2 would accept on the registry's exposure geometry (at most +0.03 per day; Appendix C).

(ii) Per-group constants that scale the hazard (rate constants, ambient diffusivity, the tube's field strength where the published solution holds it constant) are absorbed into the gamma frailty of Eq. (2). Assumption (ii) is imperfect, since a gamma frailty rescales the whole hazard while some constants enter a law non-multiplicatively, which is why we also fit a flexible area form (Section 3.2) and an observed-covariate variant, so that no rejection rests on (ii) alone. (iii) We call a mechanism *memoryless* if, under (i) and (ii), its hazard depends on the current observable state and per-group constants alone,

$$h(a) \;=\; z\,g(A(a))\,, \tag{3}$$

with z the frailty and g any function of current area, and *hidden-state* if its hazard also depends on an evolving variable that current area and per-group constants do not determine. A memoryless mechanism predicts $B = 0$ at fixed area and frailty *exactly*: once the hazard is conditioned on the current area, the time the group took to reach that area carries no further information. A hidden-state mechanism leaves an age dependence after the conditioning, with a sign and shape we derive for each mechanism, so the age term at fixed area and frailty distinguishes the two classes. Because the assumptions are ours, a rejection applies to the cast form of a law, not necessarily to the physical mechanism behind it. To reject a published casting we also require its deciding coefficient to keep the same sign under Track B (Table A3), so that no verdict depends on which histories Track A keeps. In a second adjudication we test four candidate mechanisms of our own on the same likelihood, adding covariate and stratification structure to the best-fitting shape (Appendix C.3).

We preregistered the pilot analysis and the full study, fixing the data filters, kinematic tolerances, model families, the AIC bar, and three decision criteria before the corresponding fits ran; their outcomes are in Appendix C.

3 Results

3.1 The population death rate against age

We find, from the registry's censored records, that the population's death rate falls with age (Figure 3). The points are nonparametric Turnbull estimates (Section 2.3) of the daily death hazard q_a, the probability that a group alive at age a dies within the next day (Section 2.4); this age-by-age death rate is the life table. After an infant mortality of 0.29 per day in the first day, the hazard holds at 0.118–0.137 per day through ages 2–7 and falls from age 8. The marginalized fit runs from 0.137 at age 2 to 0.070 at age 8. The registry's own fitted frailty model reproduces this fall with individuals whose risk rises (Figure 2).

Under both censoring conventions the plateau is in the data. A nonparametric estimate with the far-side matching marginalized (the diamonds of Figure 3a) holds near 0.113–0.136 per day through ages 2–7 and lies +0.022 to +0.039 per day above the marginalized gamma-Gompertz curve at ages 3–8, with the bootstrap 2.5 percent quantile above the curve at every one of those ages. To hold the plateau, a model needs an age term (Figure 3b): the paper's area, frailty, and age law holds it to within +0.010 per day of the Track A points on average at ages 3–8, against +0.043 for the marginalized gamma-Gompertz, and the model with no age term reproduces about a quarter of the excess. The comparison is within sample, and an age-only gamma-Gompertz fitted under the hard window also holds the plateau.

Among the five hazard shapes of Section 2.4 the gamma-Gompertz fit is best, with fitted parameters $h_0 = 0.459$, $B = +0.111\ \mathrm{d}^{-1}$, $\sigma^2 = 2.366$ and a population plateau $B/\sigma^2 = 0.047\ \mathrm{d}^{-1}$

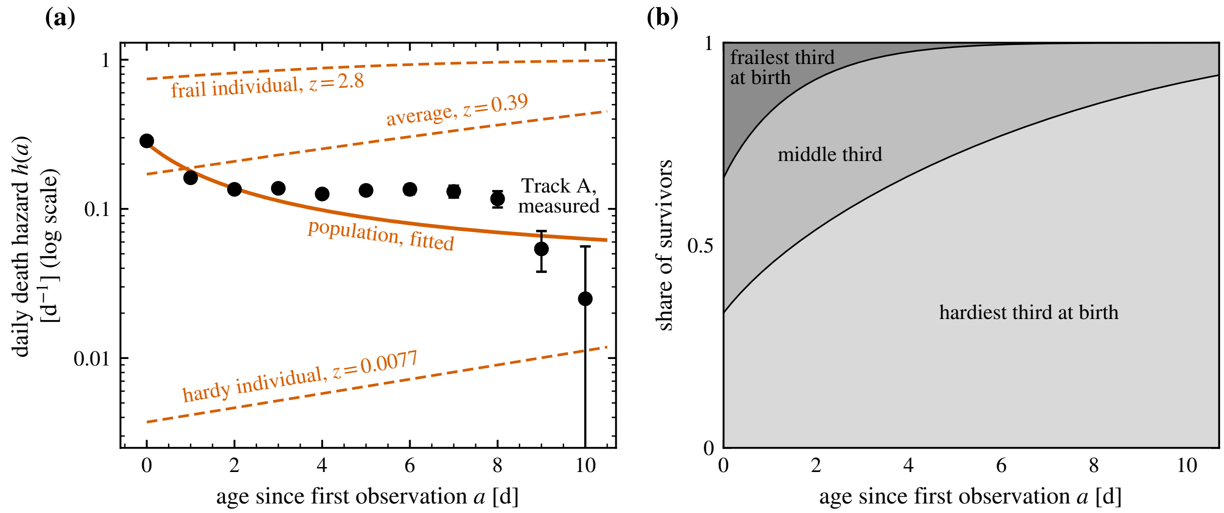

Figure 2: Every individual's risk of death rises with age while the population's falls, because the frail die first: the frailty model fitted to the Greenwich–USAF registry, drawn against that registry's measured hazard. Points in (a) are the Track A daily death hazards of Figure 3 with 95% intervals. The solid curve is the population hazard of the gamma-Gompertz model fitted with far-side matches averaged (Section 2.2), a gamma-distributed frailty multiplier z of mean 1 and variance 2.37 on one rising Gompertz hazard; the dashed curves are that law for individuals at the 10th, 50th, and 90th percentiles of the frailty. Panel (b) is the share of the survivors at each age born in the hardiest, middle, and frailest third of the frailty distribution. The solid curve falls as the points do but sits below them at ages 3–8 and above them at ages 1 and 10. The misfit comes from the parametric form, since the nonparametric hazard with matches averaged in the same way, the diamonds of Figure 3a, stays near the points.

(Table A1, Appendix B). Even with the wear-out family forced on the data the fitted population hazard falls ($\hat{B} = -0.025$ d^{-1}; Table A1). The fits on Tracks A and B, each of which fixes the far-side treatment by convention, leave Weibull and gamma-Gompertz 9.25 AIC apart on Track B, inside the bar of 10. Marginalizing the matching separates them at 166.6.

The plateau means either that every individual's hazard genuinely stops rising, which for a sunspot group could reflect the slow erosion of a finite flux reservoir, or that individuals differ, the frail die first, and the falling mixture hides individuals whose own risk still climbs. Human and insect mortality plateaus posed the same ambiguity (Section 2.3), and we adopt the resolution used there. We condition the hazard on the observable that carries the heterogeneity, here the corrected whole-spot area logged for every group on each day it stood in view.

3.2 Aging at fixed area and frailty

A group's death hazard depends on its present area, on a frailty fixed at birth, and on its age (Table 2). Present area dominates, with the hazard scaling as $(A+1)^{-1.15}$ in the full model, and residual frailty is still required at fixed area under both censoring conventions (1,868.7 AIC limb-censored, Table 2, and 3,101.6 rotation-matched). With the frailty term dropped, the same fit loses those 1,868.7 AIC and its age slope turns negative, −0.049 per day, so the rising individual risk appears only once the

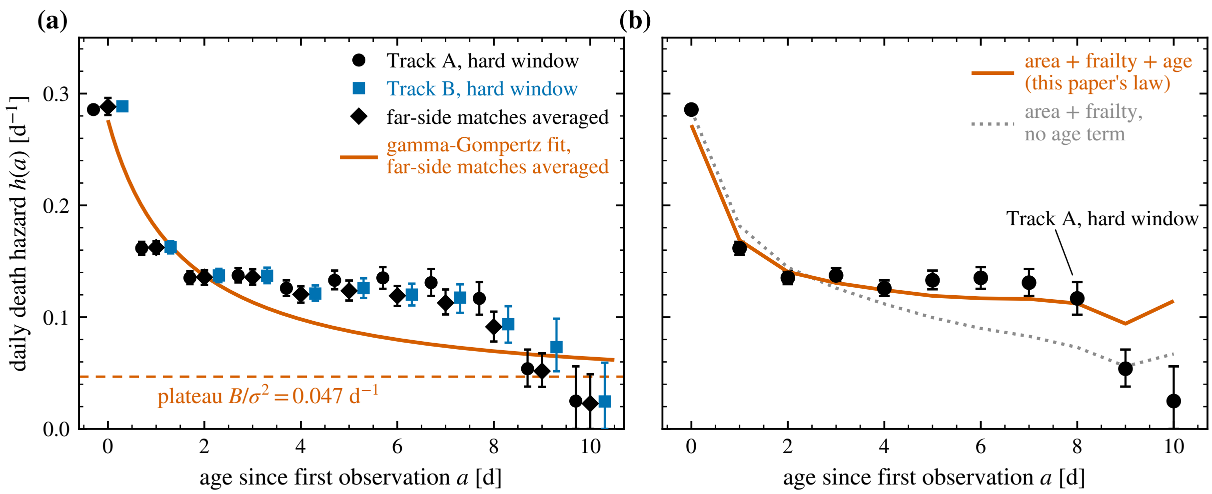

Figure 3: The death rate of sunspot groups falls with age, then holds, under both hard-window conventions and with far-side matches averaged rather than chosen; a model needs the paper's age term to hold the plateau. Daily death hazard against age, 25,883 birth-observed Greenwich–USAF histories. (a) Circles, squares: Tracks A and B, the hard-window conventions. Diamonds: far-side matches averaged over every admissible identity assignment (Section 2.2). Bars: 95% bootstrap intervals (200 block-bootstrap replicates for the diamonds; none at age 0 for the tracks). The curve, the gamma-Gompertz fit with matches averaged (plateau $B/\sigma^2 = 0.047$ d^{-1} dashed), falls below every set of points at ages 3–8, a shortfall of the parametric form itself, since the diamonds share its far-side treatment. (b) This paper's law, area with frailty and age (Eq. (2); solid), holds the plateau to within $+0.010$ d^{-1} of the Track A points on average at ages 3–8; without the age term (dotted) it falls below the plateau. The comparison in (b) is within sample, and neither line reproduces the fall at ages 9–10, both staying at or above 0.056 d^{-1}.

fit lets groups differ. The sign survives each of the other frailty shapes we fitted: two-point and three-point discrete mixtures, log-normal and inverse-Gaussian (smallest $B/\mathrm{SE} = 16.8$ in Eq. (2)). The size depends on the shape, from $+0.093$ per day under the two-point mixture to $+0.184$ under the gamma form; the three-point mixture, which the data prefer to the gamma form by 45.1 AIC, gives $+0.118$. The slope is also steeper for groups born small (Appendix B).

At fixed area and frailty the hazard of an individual group rises with age, under every area form and censoring convention fitted (Figure 4). In Eq. (2), the baseline model, the slope is $B = +0.184 \pm 0.008$ per day in log hazard, about 20 percent per day, and dropping the age term costs 601.5 AIC. The magnitude is conditional on this area form. Under a flexible area form, a natural cubic spline in $\log(A+1)$ with gamma frailty, it is $+0.115$ per day; that spline without an age term is the memoryless null against which the published castings are tested (Section 4.1). The slope stays positive when the rate and curvature of the area path, the position on the disk, or the recorded morphology and magnetic class are held fixed as well (Table A2). Multiplicative error in the recorded areas, whether 10 to 50 percent from day to day, in the size-dependent pattern measured between stations, or persistent within a group, never raises the fitted age slope of a simulated population with no aging under any of the three specifications, and lowers it or leaves it unchanged, so it cannot supply the rise (Appendix B). Out of sample, with every constant fixed

model	individual hazard $h_i(a)$	parameters	AIC − best	frailty variance σ^2
area + age + frailty	$\mathbf{z\, e^{\beta_0+\beta_1 \log(A+1)+Ba}}$	**4**	**0**	**1.163**
area + frailty	$z\, e^{\beta_0+\beta_1 \log(A+1)}$	3	601.5	0.572
area + age	$e^{\beta_0+\beta_1 \log(A+1)+Ba}$	3	1,868.7	–
area only	$e^{\beta_0+\beta_1 \log(A+1)}$	2	2,036.8	–
two-point frailty + age	$z \in \{z_1, z_2\}$, e^{β_0+Ba}	4	13,620.5	two-point
gamma-Gompertz	$z\, e^{\beta_0+Ba}$	3	13,622.1	6.646
Gompertz	e^{β_0+Ba}	2	14,560.5	–
constant	e^{β_0}	1	16,148.2	–

Table 2: Area, age, and frailty are each required: every model that drops one of them, in the rows below the bold best model, loses by far more than the decisive difference of 10 AIC. Eight discrete-time hazard models fitted to the 25,883 birth-observed histories with their daily area paths attached (95,468 group-days). The 1,868.7 margin for frailty beyond the area path decides criterion (iii) of Appendix C. Conditioning on the area path reduces the fitted frailty variance from 6.646 to 1.163, and groups at the 10th and 90th percentiles of the residual frailty still differ thirty-fold in hazard.

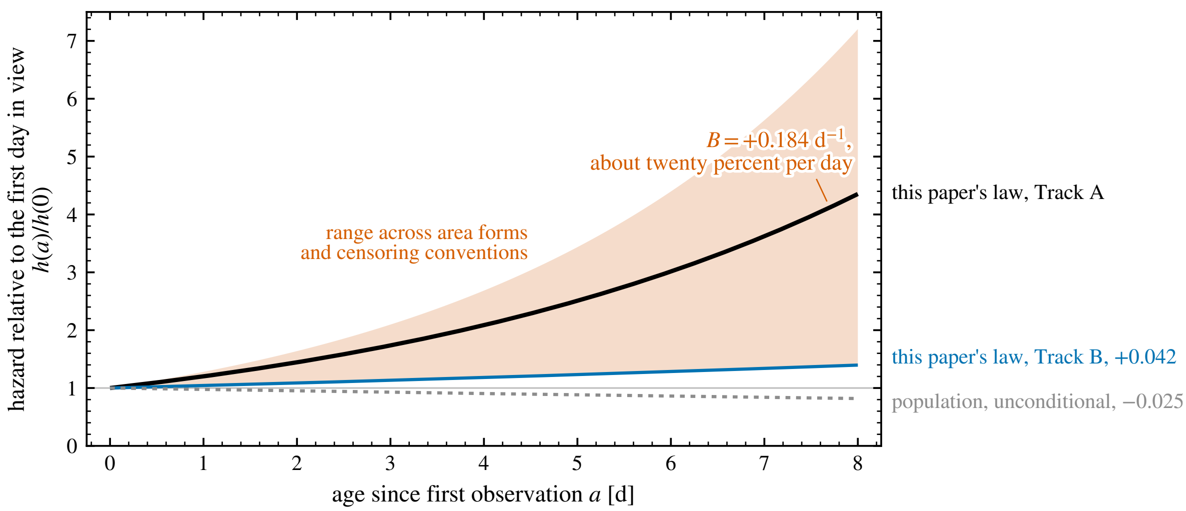

Figure 4: At fixed area and frailty the hazard of an individual sunspot group rises with age under both censoring conventions and under every area form fitted. Hazard at age a divided by the hazard on the first day in view for the same group, $h(a)/h(0) = e^{Ba}$ under the fitted age slope B, each curve named at its right end: this paper's law on Track A (black), the same law on Track B (blue), and the unconditional population slope (gray dotted). The shaded range, +0.042 to +0.247 per day, is the span of the slope across the area forms and censoring conventions fitted. The magnitude is conditional on the fitted area form; the positive sign is not.

on 1874–1953 and both models scored on 1954–2024, across the change of observing network, the model with aging fits the held-out years better by 53.8 log-likelihood points.

Age enters the size process as well: at fixed present area an older group's expected next-day

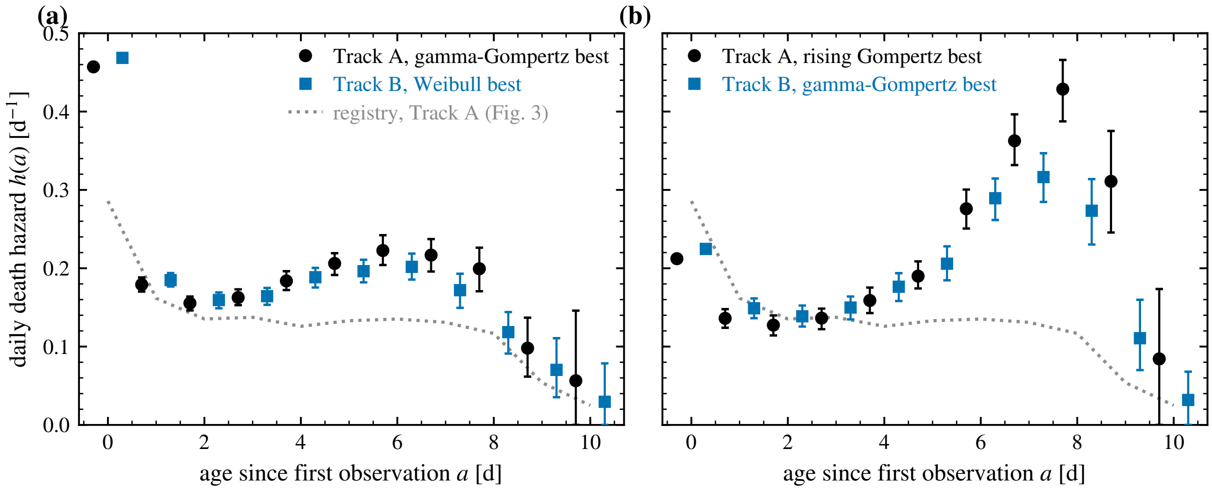

Figure 5: An independent spot-group catalog replicates the registry's falling population hazard; a magnetic-patch catalog does not. Daily death hazard on Debrecen, 1974–2018 (a), and SHARP, 2010–2024 (b), under the registry's rules: circles Track A, squares Track B, 95% bootstrap intervals (none at age 0); the gray dotted line is the registry's own Track A hazard of Figure 3. The Debrecen hazard falls as the registry's does, with a mid-life hump at ages 4–7 where the registry hazard only plateaus; SHARP's Track A hazard climbs from 0.127 to 0.429 across ages 2–8, because its recorded deaths are dispersals of whole active regions. Constant hazard is rejected by 3,774.6 and 9,647.5 AIC on the Debrecen tracks and by 199.6 and 1,269.5 on SHARP. Gompertz maximum-likelihood slopes: registry -0.150 and -0.042 d^{-1} (Tracks A, B), Debrecen -0.192 and -0.076, SHARP $+0.096$ and -0.039.

change in log area is lower by about 0.03 per day of age over ages 3–8 (1,538 AIC on 67,519 day pairs). The drift is small against the daily scatter, and a foreshortening bias could imitate it, since a group advances 13 degrees of longitude per day of age. Checks added after the main analysis that also hold the rate and curvature of the area path fixed, on the 14,109 histories that survive to age 2, still leave a rise of about 5% per day ($+0.050 \pm 0.007$, more than 7σ). Those derivatives themselves track age, so holding them fixed removes part of the effect the fit is meant to isolate. We therefore read $+0.050$ as the most conservative of the limb-censored fitted values, obtained under these controls on the recorded path, not as a bound on what a function of the true path could absorb (Section 4.2).

An older group is more likely to die than a younger group of the same size and the same frailty. Sunspot groups grow old, and the registry hides it.

3.3 Replications

The independent Debrecen spot-group catalog of Section 2.1 reproduces the registry's falling population hazard, and the Track A hazard of the SHARP magnetic-patch catalog rises instead (Figure 5). The Debrecen fits use 15,533 histories under Track A and 14,900 under Track B, and the SHARP fits use 4,537 and 4,154. On Debrecen a decelerating family fits best on each track (gamma-Gompertz on Track A, Weibull on Track B). The aging law is also reproduced on

Debrecen's own daily areas: with Eq. (2) fitted to them, dropping the age term costs 413.4 AIC, and the slope is $B = +0.231 \pm 0.014$ per day against +0.184 on the registry. Treating the catalog's intermittent-phase days as zero area, instead of interpolating them in $\log(A+1)$ under the registry's rule, gives $+0.132 \pm 0.013$ with a gain of 122.9 AIC from the age term, so the age term is required under either treatment. That coding fits worse overall by 3,923 AIC. The population hazard implied by the Debrecen-fitted law falls from age 2 to 8 and lies 0.036 per day on average below the catalog's points at ages 3–8. Neither it nor the registry-fitted law reproduces Debrecen's mid-life hump (Figure 5a).

For the SHARP catalog of HMI active-region patches (HARPs; Section 2.1) the best-fitting family on Track A is a rising Gompertz, $B = +0.096\ \mathrm{d}^{-1}$, while on Track B the hazard decelerates as in the spot catalogs (Figure 5b). A HARP's recorded death is the dispersal of the whole active region, including the plage that outlives the spots. Magnetic-patch demography is therefore a different measurement from spot-group demography, and we report the two separately. For HARP death itself the aging test has power 1.00, and dropping the age term from the flexible area form costs 1,761.58 AIC, with an age slope of +0.386 per day. A cohort of HARPs matched to the registry's spot groups had power 0.30, below the 0.5 minimum fixed in advance (even odds of detecting the planted effect), so we draw no conclusion from its null result.

3.4 Identity error and the aging slope

A recorded death may be a group the observers lost while it still lived, and since groups shrink toward death, such false deaths land late in life and would mimic aging. We measure how often the modern telescope network loses a living group and show that losses at that rate cannot produce the slope we measure. Before the run we set the rule that losses able to produce a slope of 0.184 per day would withdraw the law. We build a loss operator from the loss rates measured in the modern era of the registry and pass simulated lifetimes with no aging (age slope zero, Eq. (3)) through it at its most damaging setting, in which each measured miss is a full identity break (Appendix D).

In the USAF/NOAA era of the registry, recorded by the Solar Optical Observing Network (SOON), we count the observers' losses of living groups directly, as gaps in each group's run of daily records. Within the 7,411 SOON-era Track-A histories the observers miss a living group on 7.5 percent of interior days (days between two recorded observations of the same group), and 98.6 percent of SOON-era deaths have a last observed area below 50 MSH, the sizes at which those misses occur. The Debrecen catalog shares the registry's NOAA group numbering; over the 1977–2018 overlap 3,470 recorded on-disk deaths have a Debrecen observing day inside the death interval, and in 19.9 percent of them (689; 95% interval 18.6 to 21.2 percent) Debrecen still lists the group on such a day; because Debrecen's own sensitivity is limited, this fraction is a lower bound (Appendix D). On the SOON-era histories the real daily records give $B = +0.134$, below the registry-wide +0.184 of Eq. (2) (Table 2). Passed through the measured operator and fitted the same way, sixty simulated populations with no aging give slopes of at most +0.036 per day (mean +0.017), and at most +0.038 in three runs with every loss rate doubled, against +0.134 on the real records. With a true $B = +0.184$ planted, the same fit returns +0.038 without the operator and +0.078 with it. The censoring conventions of this SOON-only fit lower both planted slopes and the losses raise them, by +0.040 on the aging population and +0.068 on the memoryless one, so losses followed by re-entry at the measured rates add to a fitted slope rather than lowering it (Appendix D). A variant in which each loss ends the recorded history outright, with the loss rate set so that false deaths are as frequent as the Debrecen comparison allows at the upper end of its interval, leaves the slope at its loss-free value, negative in each of twenty repetitions (mean -0.046, against -0.051 with no losses; largest -0.027). No loss process in the family tested therefore reaches the measured slope (Appendix D).

Only after 1982 does the registry record how many spots a group contains. More member spots at fixed total area lower the hazard (log-count coefficient -0.458 on Track A), and a neighboring group born within 5 degrees in the previous three days raises it by about 27 percent. Conditioning on member count as well as area absorbs 0.10 of the age term's evidence on Track A (bootstrap interval 0.05 to 0.14) and 0.19 on Track B (interval -0.04 to 0.46, which bounds it only loosely). On the registry alone, the age term is still required at fixed member count, so the recorded spot count is not the hidden state that produces it. Composition finer than that count is not excluded as the state beyond current area that the slope demands.

3.5 The reversal window

We find that aging speeds up inside a window that opens near each cycle maximum, as the polar field reverses, and fades from the maximum over about two years (Figure 6); this modulation is a fit made outside the preregistered design of the study. A coarse split of the Track-A slope by cycle phase, with an era term so that the Greenwich–USAF network change is not mistaken for a phase dependence, gives 0.126 per day near minimum, 0.158 near maximum, and 0.172 on the mid-cycle flanks. The bins are two years either side of each minimum and maximum. The three-bin split improves the fit by 14.3 AIC over a single slope, and it holds under calendar-block controls (0.124, 0.151, 0.166). The calendar blocks absorb calendar-time variation in mortality due to observing cadence, catalog gaps, and seasonal or observer structure. The phase dependence rests on the mid-cycle excess: the mid-cycle-to-minimum gap of 0.046 per day exceeds the 99th percentile of the permutation null distribution, 0.042, while the minimum-to-maximum gap of 0.032 falls below it. The same ordering appears on Track B, but with no AIC support, so the cycle-keyed results here come from Track A alone. We fit the enhancement as a window that opens near each polar-field reversal, no earlier than the cycle's maximum, and closes at the next activity minimum. We measure the onset against the epoch of completed reversal, the mean of the two hemispheres' final polar-field sign changes (Section 2.1). The fitted onset falls 1.0 year before that epoch (95% interval 2.1 to 0.2 years before), which places it at the cycle's maximum or within about a year after it. The interval excludes an onset at the completed reversal itself, a preference that rests mainly on cycle 21, and it also excludes the preregistered lag band of 1.1 to 5.5 years after that epoch. With the onset held at the reversal epoch, which is the form used in the rest of the paper, the enhancement decays after the maximum with an e-folding time of 2.25 ± 0.42 years and amplitude $k = 0.210 \pm 0.034$ (Figure 6). The enhancement is an additive increment to the age slope, in the same per-day units as the slope itself (+0.135 per day outside the window in this fit). A comparison of birth cohorts, independent of any window fit, shows the same switch. Groups born within 1.5 years after the mean polar field's initial zero crossing (or after cycle maximum plus 0.75 years, where no polar record exists) age faster than groups born within 1.5 years before it, 0.185 against 0.139 per day, a contrast 13.2 standard errors from zero. The window fit rests on the post-1954 registry, where the reversal epochs are measured for each hemisphere (Section 2.1); the cohort comparison also uses the earlier cycles, with cycle maximum plus 0.75 years as the proxy epoch. The pre-1954 registry is consistent with the same modulation at reduced tracking quality.

The fade time of about two years matches how fast solar activity itself declines: after the maximum of each of cycles 19 to 24 the smoothed sunspot number (SILSO World Data Center, 2026;

Clette et al., 2014; Clette and Lefèvre, 2016) fell by a factor of e in 1.33 (cycle 24) to 3.11 (cycle 20) years, so the window closes as the cycle's activity decays. We chose the window's functional form from six pre-declared decay forms (exponential, linear and power-law decays clocked from the reversal; exponential and linear decays in cycle phase from maximum; and an exponential in years from maximum) and revised it once, after the first choice missed cycle 25 at 2.7 standard errors, so the gated exponential is a form selected partly by that data. Cycle 25, the first cycle observed inside a window before its maximum, showed weak modulation there, so in the revised form the decay is clocked from the maximum. A hemisphere-split fit is worse by 0.97 AIC and couplings to the local pole's field are rejected, so both hemispheres carry the enhancement together. The amplitude varies from cycle to cycle: dropping the differences beyond the shared profile costs 41.8 AIC (Figure 6). Cycle 24's amplitude, however, depends on the estimator: +0.150 under the full frailty and death-window estimator, near zero under passage-scoped estimators on both registries, and mildly negative on the independent Kislovodsk catalog, a roughly 3 sigma tension under the same estimator. The cycle 20 amplitude drawn in Figure 6 is negative, and that cycle's increment stays negative inside its own window under each estimator we fitted. With the onset held at the reversal epoch, its window opens 2.18 years after the cycle's maximum, later than any other cycle's. Dropping the decay inside the window costs 47.7 AIC. When each cycle has its own amplitude at maximum and the six cycles share one decline in cycle phase, a positive amplitude at cycle 20's maximum extrapolates to negative values that far into the window. With the window geometry controlled in this way, the two extremes, cycles 24 and 20, still differ by 4.7 sigma. Under that

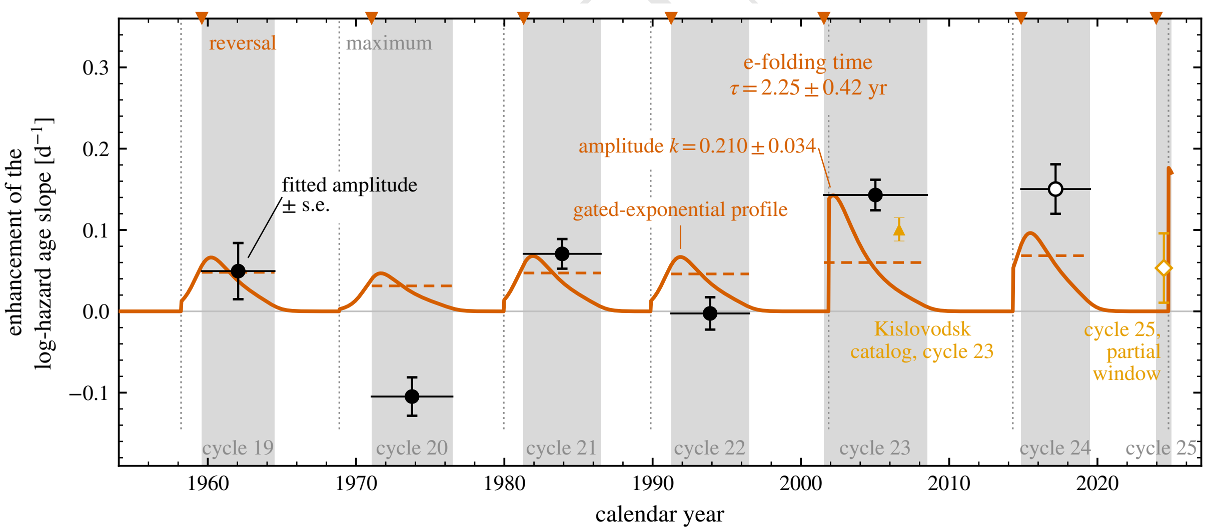

Figure 6: Aging speeds up in a window that opens near each cycle maximum, as the polar field reverses, and fades from the maximum over about two years, in fits outside the preregistered design: on the post-1954 registry, Track A, the fitted window profile against the per-cycle amplitudes of cycles 19–24, with the cycle 25 partial window and the Kislovodsk cycle 23 value. Triangles mark the reversal epochs of Section 2.1, dotted lines the cycle maxima, and gray bands each window as drawn with its onset held at the reversal epoch, to the next minimum; the fitted onset falls about a year earlier (see text). Cycle 24 is drawn open because its amplitude depends on the estimator (see text).

control each of the six amplitudes, extrapolated to its cycle's maximum, is positive, with mean $+0.18 \pm 0.02$ per day, and a new cycle is expected between $+0.09$ and $+0.27$ if the six are treated as independent, or between -0.07 and $+0.44$ allowing for their shared calibration error. An alternative tabulation of the cycle-maximum epochs shifts the six per-cycle amplitudes of Figure 6 together by about $+0.07$ and moves the cycle 24 minus cycle 20 contrast under that geometry control from 0.222 to 0.194, six tenths of its standard error.

4 The physical picture

4.1 The candidate model

Whatever destroys a spot group must know how old it is: under the bridge assumptions of Section 2.4 all memoryless forms fall, the six published mechanisms as cast among them (Table A3), by 245.63 AIC for the class as a whole against a flexible memoryless null, and the aging slope stands. The scope of that failure is the tested class: among hazard laws memoryless in current observed area under the stated bridge, none survives, and the slope requires state beyond current area. The registry's areas and positions do not say which physical variable carries that state (Section 4.2). Of 17 aging casts of our own, one was not eliminated; four others were the candidates of the second adjudication (Section 2.4), whose eight tests ended in two rejections, one withdrawal, one test that could not run as designed, and no candidate established (Table A4). Which candidate carries the state is not decided here, and telling the candidates apart is work for data beyond the registry. None of the 49 modulation candidates, carriers, and covariates we took from the literature or cast ourselves was established either, the bar being to match the best-fitting shape on both tracks with fewer or physically bounded parameters.

The one cast not eliminated does not fit as derived: the hazard form derived from its premise falls short of the free phenomenological shape by 113.7 AIC on Track A and 528.3 on Track B, past the same decisive difference of 10 that rejects the published castings. That cast is threshold collapse at a deep anchor. Unlike the memoryless castings it keeps the aging slope, and its deficit lies in one constraint of its premise per track; with that constraint relaxed it matches the free shape within the bar (see the comparison below). Section 4.2 develops it as a physical hypothesis consistent with the measured law, not one the registry establishes. In that hypothesis a group dies when turbulent erosion thins its subsurface root past its breaking point. A fitted cycle layer speeds the aging inside the window that opens near each cycle maximum, as the polar field reverses, by an amount that varies from cycle to cycle.

For group i at age a, current area A, and calendar time t, the model's hazard is

$$h_i(a, A, t) \;=\; z_i\, f(A)\, \exp\bigl\{[\,B + k\, w(t)\,]\, a\bigr\}, \tag{4}$$

where z_i is the frailty, $f(A)$ the area term, B the age slope, and $k\,w(t)$ the window layer. The profile $w(t)$ is zero outside the window of Section 3.5 and, inside it, a decaying exponential clocked from cycle maximum. The layer's fitted amplitude, $k = 0.210 \pm 0.034$ (Section 3.5), more than doubles the aging slope at the cycle maximum from which its decay is clocked.

The hazard form derived from the erosion premise in Section 4.2, Eq. (8), improves by 219.3 AIC on Track A and 329.6 on Track B on the rejected finite-reservoir cast it grew from, and with one constraint relaxed per convention it matches the free phenomenological shape with the same window term to within 1.4 and 5.8 AIC. As derived, the form fails on one constraint per track:

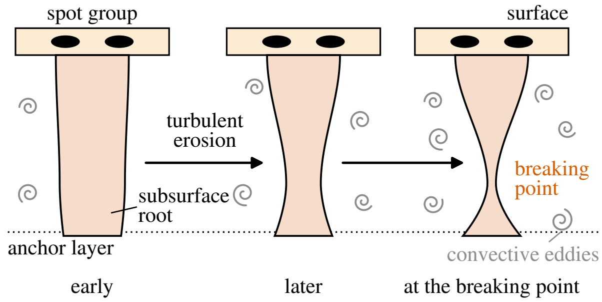

Figure 7: Schematic of the eroding-root hypothesis (no data; depths and rates not to scale): a group's subsurface root, anchored at depth, is thinned by turbulent erosion until it breaks, so the risk of collapse rises with every day survived, the rising-risk law of Section 3.2. This is the casting the measurements support, not established physics (Section 4.2).

Track A rejects the sign of its early transient, since newborn groups die faster than the aging law alone predicts for about a day after emergence, and with that excess fitted the flexible-form slope is $+0.160 \pm 0.012$ per day, inside the range the premise allows. Track B rejects the slope range, its free slope of $+0.038$ lying below the 0.13 per day the premise requires.

Calibrated on earlier cycles and scored on later ones without refitting, the window layer does not outperform a phenomenological comparator with free aging slopes in three cycle-phase bins. Cycle 25 was used in the one revision of the profile (Section 3.5); its partial pre-maximum window gives $+0.053 \pm 0.043$ under the full estimator, against the profile's predicted $+0.039$. Cycle 26 will provide the first out-of-sample test (Section 5). The Kislovodsk catalog replicates the cycle 23 amplitude at $+0.101 \pm 0.014$ and $+0.124 \pm 0.014$ under the two fit variants, a 7–9 sigma detection, and under an estimator common to both catalogs, rather than the full estimator of Section 3.5, it matches the Greenwich–USAF value of $+0.112 \pm 0.016$ at 0.5 sigma (Figure 6).

The preregistered study failed two of its three criteria and met the third, frailty beyond the area path (Appendix C); the age term at fixed area and frailty was a preregistered secondary output of the area-conditioned fits, not a criterion. On the frozen wording, the study-level preregistered verdict is therefore undecided. Our conclusions, the age term of Sections 3.2–3.4 against which the memoryless laws fail and the reversal window found afterwards and outside the preregistered design, are narrower than the question those criteria address and do not depend on their outcome.

4.2 The eroding root

The eroding root is a physical hypothesis that the measurements constrain but do not establish. The life table and hazard fits of Section 3 constrain the physics of sunspot death, first through an age term at fixed area and frailty, $+0.184$ per day in log hazard under the linear-in-$\log(A+1)$ area form (Section 3.2). Its existence and positive sign hold on both censoring tracks and under the three area forms fitted, while its magnitude is conditional on the fitted area form, running from $+0.042$ to $+0.247$ (Figure 4), and on the frailty shape, running from $+0.093$ to $+0.184$ under the preregistered area form (Section 3.2). The constraint we carry into the physics is therefore the existence and sign of the age term at fixed present state, however that state is specified, once the fit lets groups differ in frailty. Its size in the preregistered form is $+0.184$ per day, and the 5% of Section 3.2, obtained on the limb-censored histories with the rate and curvature of the recorded area path also held fixed, is the smallest value those controls give. The age term is larger than registry bookkeeping can produce. At matched conventions the measured slope, +0.134 per day, is 3.8 times the largest slope (+0.036) fitted to any of sixty simulated populations with no aging passed through the modern network's measured losses of small faint groups, and those losses raise a fitted slope rather than lower it (Section 3.4). The second constraint is the faster aging inside the window of Section 3.5, which opens near each cycle maximum as the polar field reverses; it was measured outside the preregistered design, on the post-1954 registry and on the limb-censored histories.

A sunspot group is the visible top of a bundle of magnetic flux that has risen through the convection zone, and most of it lies below the surface. Magnetic tension and twist hold the bundle together, and a converging downdraft clamps its tubes into one spot (Parker, 1979). An account of why a group dies must say which part fails, and the two measurements of Section 3, the falling population death rate and the rising individual risk at fixed area, put two conditions on the answer.

The first condition is that groups differ from one another from birth, each by a fixed factor in hazard: the frailty z_i of Eq. (4), drawn once per group (the registry's unit; it does not follow individual spots) and multiplying the common dependence on area and age without itself changing. Across groups z_i is a random variable, taken in the fits to be gamma-distributed with unit mean; its fitted variance is $\sigma^2 = 1.16$ in the area-conditioned model (Section 3.2). A two-point mixture fits the age-only data as well as the gamma form (Section 4.3), but with the area path conditioned on, the registry prefers a three-point mixture to the gamma, and the width of the spread depends on the shape assumed (Section 3.2; Appendix B). The frailest die first, and the spread is wide: thirty-fold in hazard between the 10th and 90th frailty percentiles at equal area and age under the fitted gamma form. A group of given area should be born hardier if it carries more flux, since active-region lifetimes scale with flux (Harvey and Zwaan, 1993; van Driel-Gesztelyi and Green, 2015), or if its field is more compact (Solanki, 2003), more twisted (Longcope and Welsch, 2000), or rooted in a persistent downdraft (Chen et al., 2017; Hotta and Iijima, 2020). Composition is part of that hardiness on the registry's own evidence, since more member spots at fixed total area lower the hazard (Section 3.4). Neither area nor member count exhausts the difference, so whatever kills a group acts on groups already unequal in more than the daily records show.

The second condition is that each group carries an internal state that advances with age. The hazard still rises with age at fixed rate of change of area, at fixed disk position, and at late ages (Section 3.2; Table A3). Regrowth past an old maximum steepens the dependence instead of resetting it (Table A4). Its sign, its rate, and its persistence across the nine days or so a disk passage allows require a quantity that degrades toward a threshold on that timescale (Gavrilov and Gavrilova, 2001). We call it the group's memory, without committing to what carries it.

Of the surface effects, the two that remove flux at the photosphere do not carry the group's memory in the forms we cast (Section 2.4). The moat outflow strips flux off the spot as moving magnetic features (Harvey and Harvey, 1973; Meyer et al., 1974; Hagenaar and Shine, 2005; Kubo et al., 2008) and the granulation erodes the tube's boundary (Petrovay and Moreno-Insertis, 1997; Petrovay and van Driel-Gesztelyi, 1997). Both act through the boundary of each member spot. A group's total perimeter is not fixed by its total area, since the same area split among more spots has more boundary; where the registry records the member count we condition on it as well, and the age term survives, though composition finer than the count is not controlled (Section 3.4). Neither process, as cast, supplies a quantity that accumulates from one day to the next. The turbulent-erosion law tested as P1 in Table A3 is this boundary erosion, while ours acts on the root below (Section 4.1). The flux already shed into the moat does accumulate over a group's life and could carry the memory. On the registry that history integral does not absorb the age term, and the slope does not rise with a group's mean shed rate (Table A4). One surface effect we have not cast as a carrier is the group's magnetic neighborhood: Petrovay et al. (1999) found that a spot's deviation from the mean decay law persists for about three days and is associated with the plage flux around it. Decay rates so correlated, at the amplitude they measured, produce no age term that our criterion would accept (Section 2.4; Appendix C.2), but the neighborhood flux itself, only part of which the group shed, is a candidate state our castings leave out; the shed-flux integral tests the shed part alone.

The near-surface flows below the photosphere offer clocks that do run at fixed area, winding the tube toward its kink limit, tilting it toward disconnection, or weakening the downdraft that clamps it. We cast those as death-risk laws too. Of the aging casts we tried, one was not eliminated, threshold collapse at a deep anchor; the tests it passed bear on its core, the age term of Eq. (4), and Section 4.1 compares its full derived form with the free shape. Emergence itself, which lasts a day to several days (Harvey and Zwaan, 1993; Cheung and Isobe, 2014), could produce an age dependence with no internal clock at all. A young group of given area is then still being fed and an old one is not, so the hazard should rise and saturate, and one disk passage cannot separate a saturating rise from a continuing one (Table A4).

The eroding-root model meets both conditions with one ingredient: each group has a root anchored below the moat's reach, which turbulence thins until it breaks (Section 4.1; Figure 7). The margin between the root and its breaking point at emergence would be the hardiness, the multiplier z_i of Eq. (4), and the thinning already done by a given age would be the memory. Three assumptions about the root turn that premise into the hazard law of Eq. (4). In the model magnetic tension holds the bundle to its anchor, and the group lives while enough flux stays connected there. Let M be the margin, the flux connected at the anchor beyond the least that holds the bundle, a hidden state in the sense of Section 2.4, and let M_0 be its value at emergence. We assume first that eddies at the anchor depth reconnect the bundle's flux into the surrounding field a ribbon at a time, in many small reconnections per turnover, at the pace the flow delivers them, whatever the bundle's state. The margin then falls at a steady mean rate c,

$$M(a) \;=\; M_0 \;-\; c\,a, \tag{5}$$

with a the age and c fixed by how much flux the eddies strip in one turnover time $\tau_{\rm c}$ at that depth.

This steady drain alone would fix the age at death, $a \simeq M_0/c$, a clock wound at birth of the kind rejected in Table A3. We assume second that rarer coherent encounters, distinct from the steady reconnection that drains the margin, strike the root at random at a rate ν with strengths Φ. The group dies at the first encounter stronger than the margin that remains. We assume third that the strengths are exponentially distributed with mean Φ_*, $\Pr[\Phi > x] = e^{-x/\Phi_*}$. The hazard is then the rate of encounters that exceed the margin, the construction of the Strehler–Mildvan theory of mortality, in which a linearly declining vitality meets random challenges of exponentially distributed strength (Strehler and Mildvan, 1960),

$$h(a) \;=\; \nu\,\Pr[\Phi > M(a)] \;=\; \nu\,e^{-M(a)/\Phi_*}, \tag{6}$$

and with Eq. (5), for group i at fixed area,

$$h_i(a) \;=\; \nu\,e^{-M_{0,i}/\Phi_*}\,e^{Ba}, \qquad B \;=\; \frac{c}{\Phi_*}, \qquad z_i \;\propto\; e^{-M_{0,i}/\Phi_*}. \tag{7}$$

The risk rises exactly exponentially with age for as long as margin remains, which is the Gompertz factor of Eqs. (1) and (4). The reliability theory of aging reaches the same law by other routes (Gavrilov and Gavrilova, 2001). The Strehler–Mildvan construction is indifferent to depth: any margin that declines steadily and meets challenges with an exponential tail gives the same factor, so the exponential rise fixes the form of the law and not where in the Sun the margin sits. Mixed over unequal birth margins, Eq. (7) then gives what Section 3.1 measures, a falling population death rate over members whose individual risk climbs, because the thin-margin groups die first.

The log frailty is minus the birth margin in units of the encounter scale Φ_*, so the thirty-fold spread between frailty percentiles under the gamma form is $\ln 30 \approx 3.4$ encounter scales of spread in M_0. The age slope is the drain rate in units of Φ_*. If the drain removes about one encounter scale of flux per turnover, then $c \approx \Phi_*/\tau_c$ and $B \approx 1/\tau_c$, the identification Section 4.1 assumes rather than derives. The hazard cannot exceed the encounter rate ν, since once the margin is gone every encounter kills, so at fixed frailty the rise must flatten near ν. Nine days in view have no power to detect that bend (Table A4), and groups followed longer must show it if the model is right. Area enters as a separate multiplicative factor $f(A)$ that the model does not derive. We take it from the fit and read it as the exposure of the visible spot to the surface flows.

In its first days the emerged tube is still straightening under tension and settling at its anchor, so in the model the margin departs from the line of Eq. (5) by a transient that relaxes away over a time τ_s. The window of Section 3.5 changes over years while a group lives for days, so a group born while the window is open drains faster for its whole life, and the faster rate multiplies its age. With both included, the derived form of Eq. (4) is

$$\ln h_i(a, A, t) \;=\; \ln z_i + \ln f(A) - D\, e^{-a/\tau_s} + \big[\, B + k\, w(t) \,\big]\, a, \qquad h_i \le \nu, \tag{8}$$

with D the early departure in units of Φ_*, positive for a surplus of margin and negative for a shortfall, τ_s fitted beside B, and $f(A)$ taken from the fit. The bound $h_i \le \nu$ applies to the margin factor, before it is multiplied by $f(A)$. As derived, the transient is a surplus of margin while the tube straightens, a positive D that lowers the hazard of newborn groups for a time of order τ_s. On Track A the free fit prefers the opposite sign, an early excess of hazard rather than a dip, and that sign accounts for the whole of the derived form's deficit against the free shape (Section 4.1). With the excess admitted the form matches the free shape and its slope lies inside the turnover range. We read the excess as a brief second death channel at emergence, bundles that fail before they anchor. On Track B the deficit comes instead from the slope-range constraint, since the free slope there requires a drain running at about a third of the fast-convention turnover rate at the base of the zone (Table A4).

Each of the three assumptions has an alternative with a different signature. The exponential distribution of strengths makes $\ln h$ straight in age; only its tail beyond the remaining margin matters, and a power-law tail would curve the log hazard upward toward a finite depletion time. A margin wandering diffusively with no encounters, the group dying at zero margin, would give the inverse-Gaussian lifetimes (Aalen and Gjessing, 2001) rejected for the population in Table A1. A drain that stops, because the tube disconnects early or the erodible flux runs out, freezes M and levels the hazard, the saturation one passage cannot exclude (Table A4). We measure the slope and how long the rise persists; the straightness of the log hazard beyond one passage, the form of the tail, the steady drain, and the anchor itself are assumptions.

In the model, present state and its time derivatives cannot encode the margin M. The visible area is the flux that has emerged less what the moat and the granulation have since removed, while the drain acts on the flux still tied down at the anchor and leaves no mark above until the collapse. Two groups with the same area on every day of their lives, hence the same A, $\dot{A}$ and $\ddot{A}$ today and the same earlier daily values, still differ in margin by the difference of their birth margins. Each also has less margin than its younger self at equal area, by c times the days between, so the area path fixes neither z_i nor $B\,a$. Integrating the visible trajectory from day zero does not recover M either, because the integral that matters runs over the invisible drain, $\int_0^a c\,da' = c\,a$, whose only trace at the surface is the time since emergence. A law in observed state and its derivatives can therefore absorb the age term only as far as the area path tracks age across the population, and a fit of any such law must leave a residual age term.

On the registry the age term is still needed at fixed area and at fixed first and second derivatives of area, and a flexibly specified present state leaves a smaller rise, resolved in every specification fitted (Section 3.2). The model predicts that residual: in it the visible area path is a partial proxy for age, since an older group at a given area is on average shrinking faster (Section 3.2), and for birth margin, since the survivors at a given area are the groups born with wide margins. What the proxies miss stays with age. The shed-flux history integral of Table A4 fails for the same reason: groups with the higher mean shed rate show the lower slope, the sign expected from survivorship when a long visible past marks hardiness rather than wear.

If the slope is a convective turnover rate, then under every turnover-time convention the anchor lies below the near-surface layers that overturn in hours. In mixing-length terms, convection carrying the flux F through gas of density ρ moves at about $v \simeq (F/\rho)^{1/3}$ and overturns a pressure scale height H_p in

$$\tau_\mathrm{c} \;\simeq\; \frac{H_p}{v} \;=\; H_p\Big(\frac{\rho}{F}\Big)^{1/3}. \tag{9}$$

Low in the zone, near $0.85\,R_\odot$ for instance, $F = L_\odot/4\pi r^2 \approx 9\times10^7$ W m^{-2}, $\rho \approx 40$ kg m^{-3} and $H_p \approx 40$ Mm give $v \approx 130$ m s^{-1} and $\tau_\mathrm{c} \approx 3.5$ days, so $1/\tau_\mathrm{c} \approx 0.29$ per day against the fitted slopes of $+0.042$ to $+0.247$ per day (Section 3.2). But that velocity scaling is the fast end of the turnover-time conventions in use, which differ by a factor of three to five at fixed depth, so the depth at which $1/\tau_\mathrm{c}$ meets the slope depends on the convention. Of the slopes fitted in Section 3.2, only the linear-form Track A slope, $+0.184$ per day, reaches the 0.13 per day of $1/\tau_\mathrm{c}$ at the base of the zone under the fast convention. The flexible-form slope, $+0.115$, and the Track B slopes, $+0.042$ and $+0.035$, lie below it and require a slower convention or a shallower drain. The nearest measured turbulent transport coefficient at such depths, the diffusivity of a few hundred square kilometers per second that Cameron and Schüssler (2016) inferred for subsurface toroidal flux from the butterfly diagram, is within an order of magnitude of the mixing-length value. The fits determine a rate; identifying that rate with the turnover rate at an anchoring depth is an assumption of the model, and that depth is not measured here.

Where sunspot flux is rooted is itself unsettled, and a week of memory means something different in each of the three pictures in use. In the picture that prevailed for decades, toroidal flux of order a hundred kilogauss is stored in the overshoot layer beneath the convection zone and rises as thin flux tubes (Caligari et al., 1995; Fan, 2021), whose legs would drive the polarities apart for months unless the tie is cut within days (Schüssler and Rempel, 2005). Brandenburg (2005) reads the rotation rates of magnetic tracers as favoring instead a dynamo shaped by the near-surface shear layer, which would keep spot flux shallow from the start. Global convective-dynamo simulations give a third geometry, in which toroidal structures built within the bulk of the zone shed buoyant, super-equipartition loops toward the surface (Nelson et al., 2011, 2014; Fan and Fang, 2014). Fed into a radiative simulation of the top thirty megameters, such a bundle forms a monolithic spot anchored in a persistent downdraft at that depth (Chen et al., 2017), the kind of anchor Eq. (5) assumes. Only the third supplies a structure that could carry a week of memory at fixed area; the first does so only if disconnection itself takes a week, and the second has none.

In radiative magnetohydrodynamic simulations spots are destroyed by convection from below, though no simulation reports a death hazard. In the boxes of Rempel (2011) a spot decays on about ten turnover times of its deepest layer, hours at six megameters, a day or two at sixteen, and by extrapolation a week at thirty to fifty, a third turnover convention that puts a week of memory a few tens of megameters down. The deep-domain pair of Hotta and Iijima (2020), rooted at thirty and eighty megameters, shrinks from peak area to nothing in four days, the shallower-rooted spot losing its flux first. In the emergence run of Rempel and Cheung (2014) formation passes straight into decay, two days of self-similar turbulent diffusion and then faster loss as intrusions from the deepest cells fragment the spot. These decays are smooth losses, the one feature resembling a threshold collapse being those late intrusions, and the decay studies tie a spot's life to the overturning of its deepest connected layer, as $B \simeq 1/\tau_c$ does. If the eroding root is right, such runs carried deeper and longer should show survival at fixed area falling with time since emergence and spots of equal area separating by root depth.

How early the root is cut matters most, because a severed root holds no margin to erode. In the mechanism of Schüssler and Rempel (2005), upflow along an emerged loop's legs and cooling from the surface weaken the field until convection and fluting (Meyer et al., 1977; Parker, 1979) shred the tube, two to six megameters down within three days and deeper if later, after which the hazard at fixed area should stop rising. The evidence for early disconnection is kinematic: the proper motions of a young region die out within days, and recurrent groups rotate fastest at birth and still decelerate during their second disk passage (Ruždjak et al., 2004). A third of the Dopplergram regions tracked by Švanda et al. (2009) decelerated suddenly a day or two before peak area, a cut they place tens of megameters down. Deceleration lasting into a second passage and a cut that deep fit a root that thins for a week as easily as one severed in three days.

Little would remain beneath a group severed on the third day to carry a memory a week later, and the age term is demanded at late ages and steeper after regrowth. We take these two facts to favor a connection that lasts, as in the deep-domain simulations (Chen et al., 2017; Hotta and Iijima, 2020; Fan, 2021), without excluding early disconnection. If instead disconnection is itself the slow process and Eq. (5) its progress, its completion is the death and its depth the anchor, and our fits then supply its rate and show it unfinished after nine days in view. None of this physics is established; it is the cast the measurements currently support.

Erosion by local convection alone would run at the same rate through the solar cycle. Aging instead runs faster inside the window that opens near each cycle maximum, as the polar field reverses (Section 3.5), so in this picture the root is tied to the global field. The window opens as the field changes sign, yet under the window-geometry control of Section 3.5 the amplitude extrapolated to each cycle's maximum is positive in even and odd cycles alike. The exception inside the window is cycle 20, whose window opens later after its maximum than any other and whose increment within it is negative under each estimator, so a sign change in an individual cycle is not excluded. Both hemispheres carry the enhancement together although they reverse at different times (Makarov and Sivaraman, 1986; Pishkalo, 2019; Norton et al., 2014). A carrier that sensed only the field's sign would alternate between even and odd cycles, and one confined to a polar cap would follow its own hemisphere. Since the reversals fall near the maxima, the registry does not separate a clock keyed to the reversal from one keyed to the maximum once each cycle is allowed its own amplitude (Section 3.5). The pattern thus favors an agent that is global, largely insensitive to sign, and switched on near cycle maximum as the field reverses. The reorganization of the large-scale field at reversal, as the polar holes close and re-form and the axial dipole crosses zero (Webb et al., 1984; Harvey and Recely, 2002; Hathaway, 2015), has those three properties. So does the decline of the toroidal supply, which in Babcock–Leighton models peaks near reversal and falls away on the envelope timescale (Charbonneau, 2020), cutting off fresh emergence in the nests where groups recur (Castenmiller et al., 1986). In the model either would act by speeding the drain while the window is open, the term $k\,w(t)$ of Eq. (8).

Several interior flows change at the reversal and maximum epochs and could couple the drain to the global field, though none of them yet accounts for the faster aging in the window after each cycle maximum. The zonal bands of the torsional oscillation migrate with the activity belts and sharpen the shear there, and a polar branch spins up from about maximum (Howe, 2009; Hathaway, 2015). Inflows toward the belts, strongest when activity is high, slow the meridional flow and enhance cancellation inside active regions (Cameron and Schüssler, 2012; Martin-Belda and Cameron, 2016, 2017). Both flows follow unsigned flux and span the two hemispheres, the symmetry the window shows. Cameron and Schüssler (2016) invoke a subsurface inflow of a few meters per second holding the toroidal bands together against turbulent spreading, and a root it helped confine would erode faster as that inflow weakens. But a coupling to the inflow's level predicts the largest excess near minimum and some before maximum, where we measure the slowest aging and no excess.

The two field-strength couplings we tried, to the local toroidal band and to the cycle's amplitude, both fit worse than cycle phase alone, so the modulation tracks the phase of the cycle more than the amount of field. That favors switch-like changes over a slowly weakening inflow, and the window enters Eq. (4) as a fitted layer, not as physics we have identified. Across ten covariates in a controlled comparison we found no measured property of the Sun that explains the modulation. The reconstructed polar dipole appeared to separate the cycles by window amplitude (rank correlation -0.543, exact one-sided permutation $p = 0.149$), and a control for window geometry removed the correlation (rank test $p = 0.401$, controlled correlation $+0.086$).

The depth of the anchor, the make-up of the birth margin, and the shape of the rise beyond one passage each have an instrument that would decide them. Far-side imaging (Lindsey and Braun, 2000; Liewer et al., 2017; Perri et al., 2026) follows groups past the west limb to the ages at which the hazard at fixed frailty should flatten near ν (Eq. (8)), and dates the births that occur on the far side. Because age at fixed area predicts survival, checking the model's survival forecast group by group against the Solar Orbiter far-side catalog tests the hazard law itself, separately from the pair-by-pair check of the hard-window joins (Section 5). Under early disconnection groups of equal area should look alike beneath the surface, and under an eroding root the older ones should look weaker, a difference that helioseismic imaging beneath the groups could detect (Gizon and Birch, 2005). Fits on magnetogram twist (Pevtsov et al., 2003) would test what the birth margin is made of. Emergence models face a demographic constraint as well: a convective dynamo has to deliver bundles whose root depth, flux, or downdraft differ enough to spread birth margins over the several encounter scales that the fitted hazard spread requires (Eq. (7); Appendix B). The unequal pair of Hotta and Iijima (2020) suggests the scatter exists, and scoring simulated emergences by survival at fixed area would test it.

4.3 The lifetime–area law and two populations

The three camps model a single lifetime per unit peak area, the constant α of $\tau = \alpha A_{\max}$ (Section 1). The registry does not contain that quantity: at fixed peak area the lifetime is a distribution, and the hazard–area exponent straddles inverse-linear, from -0.9 to -1.15 across the area specifications we fitted (-1.15 in the full model of Section 3.2). The scatter about $\tau = \alpha A_{\max}$ that Chaplin et al. (2026) also fitted is such a distribution of lifetimes at fixed peak area, not a dependence of risk on age at fixed current area, so their fit does not test the age term. Whether sunspot groups form two populations or a continuum is a second live dispute. Nagovitsyn, Pevtsov and collaborators have argued for two distinct populations of sunspot groups, one small and short-lived, one large and long-lived (Nagovitsyn and Pevtsov, 2016, 2021; Nagovitsyn et al., 2021), and Muraközy (2024) finds a lifetime-law break near 190 MSH. In hazard language a two-population claim is a two-point frailty mixture, which fits the age-only data as well as continuous gamma frailty: the two differ by 1.5 AIC, far below the decisive bar of 10 (Table 2). This paper is a measurement of catalogs; no claim that any published lifetime study is wrong.

In the erosion model the frailty is the spread of the groups' anchoring margins at birth and the state is the margin that remains (Eq. 7). Neither is seen from above. Conditioning on the registry's own group types, magnetic classes, spot counts and umbral fractions lowers neither the slope nor the frailty variance (Section 3.2), and whether magnetogram flux and twist or helioseismic sounding beneath groups of known age track them is the open identification. Whether composition finer than the member count carries the state beyond current area remains open (Table A4). The noise-injection test fixed in advance for the magnetic covariates of the SHARP cohort analysis (Section 3.3) remains to be run. The refit stratified on birth area and the measurement-error check on the registry's own areas are reported in Appendix B and Section 3.2.

5 Conclusions

At fixed area and frailty an older sunspot group is more likely to die than a younger one, while the population's death rate falls with age because its frailest members are removed first. Both are measurements of catalogs, and they stand whether or not the erosion model of Section 4.1 survives its forward tests. That model is our interpretation of them, a physical hypothesis the measurements admit but do not establish. In that hypothesis a group lives while its flux stays anchored below the layers that overturn in hours, and turbulent convection wears the anchor's margin down at a steady rate. The daily risk that one convective blow exceeds what remains then grows exponentially with age, at a rate we identify with the convective turnover rate at the anchoring depth, an identification the fits assume rather than measure. In the fitted cycle layer the erosion runs faster for about two years from each cycle maximum, as the polar field reverses (Section 4.2).

Far-side helioseismology has been validated against STEREO imaging (Liewer et al., 2014, 2017), and a Solar Orbiter/PHI far-side emergence catalog is being assembled (Perri et al., 2026). On the far side, the marginalized matching of Appendix A predicts an expected 5,754 far-side continuations against 3,985 hard-window joins, and a far-side catalog can check the joins pair by pair. The profile of the reversal window (Section 3.5), revised once after cycle 25, is now fixed, and cycle 26 lies outside all the fitted data. Once its reversal and maximum epochs are known, the model predicts its modulation profile with zero new parameters. Because cycle 25 was used in revising the profile, cycle 26 is the first out-of-sample test of the window layer. The prediction under test is the shared profile with $k = 0.210 \pm 0.034$, where ± 0.034 is the uncertainty of the shared amplitude alone. The six measured cycles scatter about their common level with a between-cycle standard deviation of about 0.09 per day (Section 3.5). In the convention of Figure 6, where the profile's window-averaged amplitude is about +0.05 per day, the 95% prediction interval for cycle 26's own amplitude therefore runs from −0.23 to +0.33 per day, and its sign is not predicted (Section 3.5 gives the corresponding intervals under the geometry control). Cycle 26 tests the profile and its mean level under the window-geometry control of Section 3.5, not one cycle's amplitude. Solar Orbiter's high-latitude passes begin in 2029 and cover the epochs when cycle 26's reversals are due. Both decisive measurements, the look beneath the surface and the per-hemisphere timing of the reversals, thus have instruments already flying or scheduled. We can run the same censoring-aware demography on other populations the Sun's rotation censors: the nests (recurrent emergence sites) in which spot groups appear, the plage a group leaves behind, filaments and pores, and coronal holes and active regions. The same frailty question arises for starspot catalogs, where the censoring is harsher still. The registry has held the life table for a century and a half; reading it required treating the Sun's rotation as part of the experiment.

Data and code availability

The records analyzed here are public: the Royal Greenwich Observatory and USAF/NOAA sunspot group record (Hathaway, 2024), the Debrecen Photoheliographic Data (Baranyi et al., 2016), the SDO/HMI SHARP series (Bobra et al., 2014), the Kislovodsk station catalog (Kislovodsk Mountain Astronomical Station, Pulkovo Observatory, 2026; Tlatov et al., 2014), the SDO/HMI far-side seismic maps (2010–2024) used in Appendix A, and the sunspot-number and polar-field series (SILSO World Data Center, 2026; Wilcox Solar Observatory, 2026). The analysis code and derived data will be deposited in a public repository on acceptance and are available from the authors on request until then. The deposit will contain the parsing and threading code that builds the life histories from the public registry files under both censoring conventions, with the threaded histories themselves where the source catalogs permit redistribution; the interval-censored life-table and hazard-shape fits with their bootstrap and interval-arithmetic checks. It will also contain the daily-hazard fits of Table 2 with the per-day area paths they condition on and the likelihood they maximize; the far-side matching likelihood in its three forms, exhaustive enumeration, dynamic program and beam; the replication fits on Debrecen and SHARP; the mechanism castings, the reversal-window fits and the simulation controls of Sections 3.2 and 3.4; the figure scripts; and the preregistration documents with their filing dates.

A Threading and the matching likelihood

A west-limb exit i and an east-limb reappearance j are admissible partners when the return gap is 8–18 days and the pair's implied synodic rotation rate and latitude drift are consistent with the Newton and Nunn (1951) law for recurrent groups. The 8–18 day gap admits a single far-side transit; a group that survives several transits appears as a chain of single-transit links. The rotation tolerance $\sigma_\omega = 0.73$ deg/day is the root-sum-square of 0.60 deg/day of group-to-group scatter about the mean law, 0.41 from day-quantized endpoint times over a 13.3-day gap, and 0.11 from limb position error. The latitude tolerance $\sigma_{\mathrm{lat}} = 1.4$ deg combines 0.71 deg of centroid error at the two ends with 1.2 deg of centroid wander over the 13-day passage.

Admissibility yields 19,288 edges over the segment set, falling into 3,789 connected components. Each edge carries a kinematic likelihood weight scored against a Poisson clutter rate estimated from displaced 22–32-day windows, pooled by era, latitude band, and activity tercile. The displaced window shares the return window's limb geometry and lies between the single-transit return and the double-transit return near 40 days, so it holds only unrelated east-limb appearances. We then sum the likelihood of the data exactly over complete matchings, the vertex-disjoint path covers of each component. We enumerate the smaller components exhaustively, 13.9 million matchings in all, and sum the 101 larger components by an exact dynamic program. In every matching, each east-limb reappearance is either a matched far-side continuation or a fresh emergence. A fresh emergence enters the likelihood through a stationary-age left-truncation term (a group born on the far side enters observation already aged), so every matching explains every record.

The seven components that overflow the exact dynamic program (87–338 nodes; 1,323 segments, 3.1% of all segments) are summed by a fixed-width beam (width 10^5). The beam's worst calibrated deficit, measured by running the same beam on the five largest exactly summed components, is 0.0804 nats (twice that in AIC units at equal parameter count). That deficit is negligible against the marginalized ladder's pairwise margins of at least 147.7 AIC. Table A1 has two columns because the beam sum gives only a lower bound on each over-budget component's likelihood; the preregistration fixed that a ranking differing between the columns would be reported as undecided. We departed from the preregistration in one implementation detail: the clutter normalization used a fixed $D_{ij} = 360°$ in place of the preregistered per-edge Jacobian $|\mathrm{d}\Delta t/\mathrm{d}\omega| = D_{ij}/\omega^2$ (mean $D_{ij} = 213.0°$ over the admissible edges), which puts the clutter rate at about 1.69 times its preregistered value. A rerun under the preregistered form widens every deciding margin (Weibull, 166.6 to 255.8) and narrows only the inverse-Gaussian, 2,734.8 to 2,625.8, which decides no claim, so the deviation is conservative.

We tested Track B's assumption of far-side death against the HMI far-side seismic maps (2010–2024) under a rule we fixed before reading any map, on 135 predicted survivals matched in area and date to 135 predicted non-survivals. We found a far-side detection in 93 cases among the predicted survivals (0.689) against 76 among the predicted non-survivals (0.563), a difference of +0.126 (95 percent interval 0.011 to 0.237; Fisher $p = 0.044$), which the outcome table we fixed in advance records as suggestive, not confirmed; without four controls that exit within two weeks of the catalog's end the count is 89 of 131 against 74 of 131 ($p = 0.074$). In control regions mirrored to the opposite hemisphere the same search detects a region in 0.282 of the predicted-survival pairs and 0.153 of the predicted-non-survival pairs, so the detections sit at the predicted places in both arms; the control rate itself shows that the seismic maps see a group's magnetic region whether or not its spots survive, which bounds how sharply any such test can discriminate. On this evidence the matching's predictions of far-side survival are weakly correlated with the seismic detections, in a test sample limited to the larger groups of the HMI years.

B Estimators and fits

In the area-conditioned fits of Table 2, 4,672 of the group-days are gap days whose area is interpolated, and 20,697 lie inside death intervals, between a group's last observation and its bracketed death; on 4,146 of those the fit carries the last measured area forward.

Fitted separately in terciles of the area recorded at birth (below 10, 10 to 19, and 20 or more MSH), the age slope of Eq. (2) is positive in each, $+0.458 \pm 0.034$, $+0.229 \pm 0.022$ and $+0.176 \pm 0.011$ per

model	parameters	ΔAIC (beam incl.)	ΔAIC (beam excl.)
gamma-Gompertz	3	**0**	**0**
Weibull	2	166.6	147.8
inverse-Gaussian	2	2,734.8	2,488.4
Gompertz	2	6,963.4	6,740.0
exponential	1	12,018.6	11,823.9

Table A1: AIC excess ΔAIC over the best-fitting model for five hazard shapes fitted to the registry with the far-side matching likelihood summed over the admissible identity assignments. The seven components that overflowed the exact sum are scored under the beam approximation (incl.) or dropped for every model alike (excl.; Appendix A). Gamma-Gompertz fits best in both columns, and every non-decelerating shape has an AIC higher by thousands. The beam-inclusive differences are enclosed in interval arithmetic at the fitted parameters.

day from the smallest births to the largest, so it is not produced by pooling groups born at different sizes. The 10th-to-90th percentile hazard ratio of the frailty depends on the assumed shape. It is 13 and 7 under the two- and three-point mixtures, 18 under the inverse-Gaussian form, and 31 and 32 under the gamma and log-normal forms; the thirty-fold spread quoted in Section 4 is therefore the gamma-conditional figure. Discrete mixtures with four and five support points, fitted after the preregistered set, fit better still (-69 and -76 AIC against the gamma form) and give $+0.145$ and $+0.153$ per day.

In a simulated memoryless population with zero measurement error whose hazard follows the flexible area law fitted to the registry (Table A2, third row) rather than the log-linear law, Eq. (2) reads $+0.061$ per day (positive in each of 200 simulated registries; largest $+0.088$), a third of the measured $+0.184$ and below the flexible-form $+0.115$. The flexible form reads $+0.002$ and the rate-and-curvature specification zero to three decimals (the simulated population of the position rows in that table, which gives a negative slope, follows the log-linear area law itself through the passage geometry). Day-to-day area error (standard deviation 0.1, 0.2, 0.3 and 0.5 in log area) moves the three readings to, respectively, $+0.055$, $+0.037$, $+0.011$, -0.052 (Eq. 2), -0.002, -0.015, -0.034, -0.076 (flexible) and -0.000 to -0.001 (rate and curvature). The cross-station pattern gives -0.009, -0.052 and -0.002, and a 30 percent error, half of whose variance persists within the group, gives $+0.028$, -0.018 and -0.015.

We recompute in interval arithmetic, at the reported parameters, every AIC difference on which a decision rests; the smallest deciding margin is 18.95 AIC against the bar of 10. Because the constant-hazard (exponential) interval-censored log-likelihood is concave, a tangent construction gives an upper bound on its maximum without locating it, and hence a lower bound on the AIC margin by which a constant hazard is rejected on each of the six hard-window datasets. The resulting AIC margins are at least 1,586.09 and 4,026.27 on the registry's two tracks, 1,688.26 and 5,595.64 on Debrecen, and 199.18 and 1,095.99 on the SHARPs.

specification	histories	slope B (per day)	ΔAIC
Eq. (2) *and its flexible-form variant*			
linear $\log(A+1)$, frailty, age	25,883	$+0.184 \pm 0.008$	601.5
the same, rotation-matched	24,489	+0.042	531.9
cubic spline in $\log(A+1)$, frailty, age	25,883	+0.115	–
rate and curvature of the area path held fixed as well			
quadratic $\log(A+1)$, rate and curvature of the path, age (survivors to age 2)	14,109	$+0.050 \pm 0.007$	50.4
position on the disk			
center-to-limb term; age-by-position interaction	25,883	+0.182; +0.180	–
within thirds of the birth-longitude distribution	–	+0.214 to +0.361	–
memoryless population through the registry's geometry (simulated)	–	negative	–
recorded morphology and magnetic class, added to the flexible area form			
Greenwich group type, ten classes (records through 1976)	18,472	$+0.285\pm0.012$ ($+0.139\pm0.010$ without)	858.5
umbral fraction (records through 1976)	18,472	$+0.152 \pm 0.010$	287.1
McIntosh and Mount Wilson class, spot count (records from 1982)	5,788	$+0.209\pm0.015$ ($+0.196\pm0.014$ without)	305.5
days copied forward inside death intervals, refitted three ways			
death the day after the last observation; own decay; median shrinkage	–	+0.178 to +0.184	–
the same three refits, rotation-matched	–	+0.010 to +0.038	at least 53.6
by observing era (flexible area form)			
refitted inside the Greenwich and the USAF/NOAA era	–	+0.139; +0.146	–

Table A2: Checks that the rising hazard is not an artifact of how the area term, the group's position on the disk, its recorded morphology, or the unobserved far-side days are treated: the age slope B of log hazard on age refitted under each alternative, with the AIC cost ΔAIC of dropping the age term. The slope is positive in each frailty specification and control fitted to the registry, and a memoryless population passed through the registry's own geometry and censoring gives a negative slope. Quoted $\pm$ are one standard error; ranges span the codings fitted; a dash marks a quantity not fitted or not quoted. Position, birth longitude and age are collinear, so the position rows hold two of the three fixed. The best-fitting hidden-state shape gives +0.216, a value described but not claimed (Table A3), and the parabolic-law casting +0.247, the top of the shaded range in Figure 4. Rows are limb-censored (Track A, Section 2.2) unless marked rotation-matched (Track B).

C Preregistration and its outcomes

C.1 The three criteria

(i) The hazard fitted with matching marginalized must lie inside the pilot's nonparametric confidence-band union at every age from 2 to 8. It tests whether the pilot's matching ambiguity (Section 2.2) is dissolved, with the hard-window tracks as sensitivity bounds. (ii) Both independent catalogs must replicate the decelerating shape in both censoring tracks. (iii) The area-conditioned fits of Table 2 must require frailty beyond the area path by an AIC margin that clears the bar of 10, with an enclosure proving the difference at the fitted parameters. Criterion (iii) passed (Table 2, Appendix B). But Criterion (i) failed, because the fitted hazard lies below the band at ages 3–8. Marginalization recovers about 44% more far-side continuations than the hard windows and lengthens lives, pulling the hazard plateau from the hard-window 0.13 d^{-1} down to 0.047 d^{-1}. The marginalized fit decelerates as both hard-window tracks do, but over ages 2 to 8 its hazard is inside the band union at age 2 only (Figure 3). We report Criterion (i) as failed on its as-registered wording. Criterion (ii) failed on the SHARP Track A fit: on the reading recorded before the fit, the SHARP catalog tracks a different object, the magnetic patch (Section 3.3). The criterion failed as frozen. We changed two further details of the marginalized likelihood between the replication fits and the marginalized fit; an independent reimplementation shows that both leave the estimand unchanged.

C.2 The published decay mechanisms

Table A3 maps the six castings, P1 through P6, to their results. As elsewhere, the adjudication is a measurement of catalogs: no claim that any published decay mechanism is wrong as physics. The verdict, in its mechanical form: all memoryless forms fall; aging stands. One further structure is described but not claimed, because no preregistered test attaches to it. For the parabolic law (P2), the running-maximum fit had been run once before the design freeze as an operational check, so its point estimate was known in advance; the rerun under the fixed rules reproduced that estimate. A hazard rising with raw age fits better by 587.97 AIC than one clocked by the diffusion lifetime of P3, and the fitted clock coefficient has the wrong sign (-0.23; -0.51 under Track B). The rejection rests on the AIC gap alone, because the clock coefficient flips positive when the fit is restricted to post-maximum exposure. With the logarithmic moving-boundary factor of its Eq. (16) retained rather than the constant-speed limit, the Litvinenko and Wheatland (2015) law of P1 makes a spot of given area shrink more slowly the older it is. Applied to the registry's groups it therefore predicts, at fixed area, a hazard that falls with age, from -0.046 to -0.219 per day across the preregistered diffusivity grid of 50 to 1000 $\mathrm{km}^2\,\mathrm{s}^{-1}$. The likelihood itself prefers a diffusivity below granular values, 21 $\mathrm{km}^2\,\mathrm{s}^{-1}$, where the law acts on 7 percent of group-days and the implied slope is -0.017 per day; the improved fit there disappears once groups recorded at 0 to 5 MSH are given their own levels, a check made after the fit. On the preregistered grid this form of the law fits worse than the memoryless null of Section 3.2 (the flexible area form without an age term, under which the P1 row was adjudicated) by at least 672 AIC, and worse than Eq. (2) with its age term by at least 27; the age slope that remains after conditioning on its drift is at least $+0.128$ per day. We planted, on the registry's exposure geometry, a memoryless population whose log decay rate (its log hazard, under assumption (i)) follows a three-day autoregressive process with the width Petrovay et al. (1999) measured (0.19 dex), and refitted. The spurious age slope is $+0.003$ per day under the flexible area form (99th percentile +0.026 over 200 simulated registries), and no simulated registry gives an age term the criterion would accept (largest ΔAIC 7.0 against the bar of 10 and the observed 245.63); at 2.3 times the measured width the largest of 100 is 9.3.

ID	cast decay law	class under the bridge	result for the cast form	margin (ΔAIC)
P1	turbulent erosion, theory (Petrovay and Moreno-Insertis, 1997; Litvinenko and Wheatland, 2015)	memoryless	falls with the class; cast with its full moving-boundary factor, predicts a hazard falling with age	245.63
P2	parabolic decay $D_{\mathrm{dec}} = C\, r/r_0$ (Petrovay and van Driel-Gesztelyi, 1997)	memoryless given area, running max	rejected as a complete law	585.39
P3	diffusion lifetime clock (Bradshaw and Hartigan, 2014)	hidden state, set at birth	rejected	587.97
P4	self-similar transient (Litvinenko and Wheatland, 2017)	memoryless at late age	rejected	18.95; late-age 388.78
P5	current-state laws (Gnevyshev, 1938; Waldmeier, 1955; Martínez Pillet et al., 1993)	memoryless	falls with the class	245.63
P6	structure decay, schematic	hidden state	constant-slope reading fits worse than a richer shape	39.97

Table A3: Published decay mechanisms cast as hazard-versus-age laws, with each law's class under the bridge assumptions of Section 2.4, the result for the cast form, and the AIC margin under Track A; under Track B every deciding coefficient keeps its Track-A sign. Margins are enclosed in interval arithmetic at the fitted parameters except the floating-point 39.97 (Appendix B). A rejection is a rejection of the cast form, not of the mechanism as physics, and the P6 row is described but not claimed.

C.3 The two decay-law adjudications

The second adjudication (Section 2.4) tested four of our own 17 casts (Section 4.1): a subsurface disconnection clock, a twist-relaxation clock, a penumbral boundary-erosion clock, and a shed-debris history integral (A3 in Table A4). Each test checks one prediction by which a candidate would differ from the best-fitting hazard shape on registry data; two tests bear on more than one candidate. The late-age bend of test E9, for instance, is the 15 to 30 percent downward curvature that the twist-relaxation clock requires, because in that model the hazard cannot exceed a fixed attempt rate.

test	question	deciding numbers	outcome
E6	do the candidates' rising transients have the required sign?	sign-constrained fit worse by 113.4 (Track A), by nothing (Track B)	not decided: conventions disagree
E7	does the shed-debris history integral (A3) absorb the age term?	age-slope drop 0.44 vs attainability bar 1.11	rejected as a registry claim (Track-A attainability; Track-B signs favorable)
E8a	does the age slope scale as a budget clock, $\propto 1/A_0$?	$1/A_0$ scaling fits worse than a common slope by 234.9	no rejection, no support; the slope declines with birth size, by a factor of 3.46 on corrected birth areas, and the birth-area terciles of Appendix B show the same decline
E8b	does the slope rise with a group's mean shed rate (A3)?	fitted relation -4.99; high-shed $+0.45$ below low-shed $+1.48$	rejected
E9	does the slope bend at late ages?	power 0.00: 12 of 12 simulated curved age slopes undetectable on 4,998 late-age histories	not decided: no power at this sample size
E10	does regrowth past an old maximum reset the clock?	interaction demanded at 83.6 on 1,948 regrowth histories; dependence steepens	no reset
E11	is there decay-phase structure in the slope?	fitted -0.083 vs survivorship artifact -0.086 ± 0.005 (0.6 sigma)	withdrawn: a quantified survivorship artifact
E12	is the age term group composition (last-spot death)?	preregistered parse joins 77.5% of group-days; post-1982 control: age term retains 90%/81% of its evidence at fixed area+count	not run as preregistered: pre-1982 member counts do not exist, so the full-archive test cannot be met; on the post-1982 registry, real structure but not the whole story, the age term keeping 90% (A) / 81% (B) of its evidence at fixed area and count; not decided, no decomposition claimed

Table A4: The second decay-law adjudication: no candidate hidden-state mechanism separates from the best-fitting shape on registry data alone. Each row gives one preregistered test, the numbers that decide it, and its outcome. The likelihood quantities that enter the decisions of E6, E7, E8a, E9, E10, and E11 are enclosed in interval arithmetic at the reported parameters (Appendix B), and every deciding number, the E8b bar quantities included, was reproduced to machine precision by an independent reimplementation. E7 and E8b reject only the cast forms: the history integral as a registry claim under the Track-A attainability clause, and the shed-rate relation on its bar. The attainability bar was chosen before the fit and calibrated to what the mechanism at its measured magnitudes produces through the same fitter, in place of the 50 percent drop originally written down.

D The death-versus-loss control

The registry's loss operator of Section 3.4 is the per-day probability that observers lose a living group, together with the distribution of gaps after which they find it again. We measured the operator on the SOON era of the registry, 7,411 Track-A histories and 24,245 interior days, excluding days without any catalog entries. The age slope that these losses alone produce in a simulated memoryless population therefore characterizes the modern network's bookkeeping and applies to Track A. The loss rates by area are 29.9%/day below 10 MSH; 17.7%/day at 10–20; 2.1%/day at 20–50; 0.34%/day at 50–100; 0.15%/day at 100–200; and zero at or above 200 MSH. The Debrecen fraction of Section 3.4 (20.9 percent, 19.6 to 22.3, if Debrecen's lettered sub-groups at the group's own position are also counted) tracks that catalog's own detection efficiency, from 2 percent of deaths in 1986–1996, when Debrecen records the group on its last USAF day only 13 percent of the time, to 34 percent in 2009–2018. In a check made after the count, among the 1,341 deaths for which Debrecen did record the group on its last USAF day the fraction is 44 percent (42 to 47). Of the surviving Debrecen groups, 88 percent are smaller than 10 MSH (median 3), and 70 percent are gone from Debrecen within two days of the last USAF record.

In a forward model of this control we plant simulated populations with no aging (memoryless) and with aging ($B = 0.184$, with the fitted frailty) on the real 7,411 dense area paths and observe them through the Track-A passage window. We then apply the measured operator at its most damaging setting (Section 3.4). Every measured miss is a full identity break, re-found groups re-enter as new histories with age reset, and gap lengths are drawn from the measured run-length distribution. Each repetition is re-fit with the paper's interval-censored gamma-frailty likelihood, all four parameters free.

In the memoryless-plus-operator variant the fitted B ranged from 0.0086 to 0.0241 over the six repetitions of record (mean 0.0185, sd 0.0056) and from 0.0024 to 0.0353 over sixty (mean 0.0169, sd 0.0074; one-sided 95%-content, 95%-confidence tolerance bound 0.032). In the planted-aging-plus-operator variant B ranged from 0.0581 to 0.0994 over twenty repetitions (mean 0.0778, sd 0.0110; the six of record 0.0673 to 0.0994, mean 0.0818). With the operator switched off and nothing else changed, twenty planted-aging repetitions gave 0.0227 to 0.0501 (mean 0.0378, sd 0.0073) and twenty memoryless repetitions gave -0.0608 to -0.0376 (mean -0.0514, sd 0.0065). The censoring conventions of the SOON-only fit therefore account for the whole drop from the planted 0.184, and the operator moves fitted slopes upward in both populations, by $+0.040 \pm 0.003$ with aging and $+0.068 \pm 0.002$ without. The real record's $+0.134$ exceeds the largest planted-aging replicate (0.099), so either the real per-day slope on the forward model's scale exceeds the planted 0.184 or the forward model's censoring conventions differ from the real record's, a point we leave open. With terminal losses (no re-entry) calibrated by last-area cell to the Debrecen fraction and to the upper end of its interval, twenty memoryless repetitions gave -0.066 to -0.032 (mean -0.049) and -0.057 to -0.027 (mean -0.046) respectively, and twenty planted-aging repetitions gave $+0.005$ to $+0.052$ (mean $+0.034$) and $+0.000$ to $+0.063$ (mean $+0.032$). Calibrated instead to the 44 percent found among deaths that Debrecen itself tracked (examined after the count) and to its upper limit (false deaths then 44 and 53 percent of the simulated record), they gave -0.029 to -0.009 and -0.019 to $+0.011$ respectively. With an uncalibrated loss of 12 to 40 percent of groups per day (false deaths 64 percent) the fit loses the area dependence of the hazard and the slope is no longer identified (median -0.058, 3 of 20 repetitions above $+0.134$).

References

Odd O. Aalen and Håkon K. Gjessing. Understanding the shape of the hazard rate: a process point of view. *Statistical Science*, 16(1):1–22, 2001. doi: 10.1214/ss/998929473.

H. Akaike. A new look at the statistical model identification. *IEEE Transactions on Automatic Control*, 19(6):716–723, 1974. doi: 10.1109/TAC.1974.1100705.

T. Baranyi, L. Győri, and A. Ludmány. On-line tools for solar data compiled at the Debrecen Observatory and their extensions with the Greenwich sunspot data. *Solar Physics*, 291:3081–3102, 2016. doi: 10.1007/s11207-016-0930-1. arXiv:1606.00669.

Gibor Basri, Tristan Streichenberger, Connor McWard, Lawrence Edmond, IV, Joanne Tan, Minjoo Lee, and Trey Melton. A new method for estimating starspot lifetimes based on autocorrelation functions. *The Astrophysical Journal*, 924:31, 2022. doi: 10.3847/1538-4357/ac3420.

M. G. Bobra, X. Sun, J. T. Hoeksema, M. Turmon, Y. Liu, K. Hayashi, G. Barnes, and K. D. Leka. The helioseismic and magnetic imager (HMI) vector magnetic field pipeline: SHARPs – space-weather HMI active region patches. *Solar Physics*, 289:3549–3578, 2014. doi: 10.1007/s11207-014-0529-3.

S. J. Bradshaw and P. Hartigan. On sunspot and starspot lifetimes. *The Astrophysical Journal*, 795:79, 2014. doi: 10.1088/0004-637X/795/1/79. arXiv:1409.4337.

A. Brandenburg. The case for a distributed solar dynamo shaped by near-surface shear. *The Astrophysical Journal*, 625:539–547, 2005. doi: 10.1086/429584. arXiv:astro-ph/0502275.

Kenneth P. Burnham and David R. Anderson. *Model Selection and Multimodel Inference: A Practical Information-Theoretic Approach*. Springer, New York, 2 edition, 2002. doi: 10.1007/b97636.

P. Caligari, F. Moreno-Insertis, and M. Schüssler. Emerging flux tubes in the solar convection zone. I. Asymmetry, tilt, and emergence latitude. *The Astrophysical Journal*, 441:886, 1995. doi: 10.1086/175410.

R. H. Cameron and M. Schüssler. Are the strengths of solar cycles determined by converging flows towards the activity belts? *Astronomy & Astrophysics*, 548:A57, 2012. doi: 10.1051/0004-6361/201219914. arXiv:1210.7644.

R. H. Cameron and M. Schüssler. The turbulent diffusion of toroidal magnetic flux as inferred from properties of the sunspot butterfly diagram. *Astronomy & Astrophysics*, 591:A46, 2016. doi: 10.1051/0004-6361/201527284. arXiv:1604.07340.

J. R. Carey, P. Liedo, D. Orozco, and J. W. Vaupel. Slowing of mortality rates at older ages in large medfly cohorts. *Science*, 258(5081):457–461, 1992. doi: 10.1126/science.1411540.

M. J. M. Castenmiller, C. Zwaan, and E. B. J. van der Zalm. Sunspot nests. *Solar Physics*, 105:237–255, 1986. doi: 10.1007/BF00172045.

W. J. Chaplin, R. Howe, S. Basu, Y. Elsworth, S. J. Hale, E. J. Hatt, E. Murray, and M. B. Nielsen. Constraints on sunspot group lifetimes from far-side Sun-as-a-star helioseismology with BiSON. *Monthly Notices of the Royal Astronomical Society*, 546(1):staf2287, 2026. doi: 10.1093/mnras/staf2287. arXiv:2601.02153.

P. Charbonneau. Dynamo models of the solar cycle. *Living Reviews in Solar Physics*, 17:4, 2020. doi: 10.1007/s41116-020-00025-6.

F. Chen, M. Rempel, and Y. Fan. Emergence of magnetic flux generated in a solar convective dynamo. I. The formation of sunspots and active regions, and the origin of their asymmetries. *The Astrophysical Journal*, 846:149, 2017. doi: 10.3847/1538-4357/aa85a0. arXiv:1704.05999.

M. C. M. Cheung and H. Isobe. Flux emergence (theory). *Living Reviews in Solar Physics*, 11:3, 2014. doi: 10.12942/lrsp-2014-3.

F. Clette and L. Lefèvre. The new sunspot number: Assembling all corrections. *Solar Physics*, 291: 2629–2651, 2016. doi: 10.1007/s11207-016-1014-y.

F. Clette, L. Svalgaard, J. M. Vaquero, and E. W. Cliver. Revisiting the sunspot number. *Space Science Reviews*, 186:35–103, 2014. doi: 10.1007/s11214-014-0074-2.

D. R. Cox. Regression models and life-tables. *Journal of the Royal Statistical Society: Series B (Methodological)*, 34(2):187–202, 1972. doi: 10.1111/j.2517-6161.1972.tb00899.x.

I. Dakanalis, G. Tsiropoula, K. Tziotziou, and I. Kontogiannis. Chromospheric swirls. I. Automated detection in Hα observations and their statistical properties. *Astronomy & Astrophysics*, 663: A94, 2022. doi: 10.1051/0004-6361/202243236. arXiv:2205.07720.

Bradley Efron and Robert J. Tibshirani. *An Introduction to the Bootstrap*. Chapman & Hall/CRC, New York, 1993. doi: 10.1007/978-1-4899-4541-9.

Y. Fan. Magnetic fields in the solar convection zone. *Living Reviews in Solar Physics*, 18:5, 2021. doi: 10.1007/s41116-021-00031-2.

Y. Fan and F. Fang. A simulation of convective dynamo in the solar convective envelope: Maintenance of the solar-like differential rotation and emerging flux. *The Astrophysical Journal*, 789:35, 2014. doi: 10.1088/0004-637X/789/1/35. arXiv:1405.3926.

E. D. Feigelson and P. I. Nelson. Statistical methods for astronomical data with upper limits. I. Univariate distributions. *The Astrophysical Journal*, 293:192–206, 1985. doi: 10.1086/163225.

E. Forgács-Dajka, L. Dobos, and I. Ballai. Time-dependent properties of sunspot groups. I. Lifetime and asymmetric evolution. *Astronomy & Astrophysics*, 653:A50, 2021. doi: 10.1051/0004-6361/202140731. arXiv:2106.04917.

L. A. Gavrilov and N. S. Gavrilova. The reliability theory of aging and longevity. *Journal of Theoretical Biology*, 213:527–545, 2001. doi: 10.1006/jtbi.2001.2430.

Helen A. C. Giles, Andrew Collier Cameron, and Raphaëlle D. Haywood. A Kepler study of starspot lifetimes with respect to light-curve amplitude and spectral type. *Monthly Notices of the Royal Astronomical Society*, 472:1618, 2017. doi: 10.1093/mnras/stx1931.

L. Gizon and A. C. Birch. Local helioseismology. *Living Reviews in Solar Physics*, 2:6, 2005. doi: 10.12942/lrsp-2005-6.

M. N. Gnevyshev. On the nature of solar activity. *Izvestiya Glavnoi Astronomicheskoi Observatorii v Pulkove*, 16:36–45, 1938. Also cited as Pulkovo Obs. Circ. 24, 37.

B. Gompertz. On the nature of the function expressive of the law of human mortality, and on a new mode of determining the value of life contingencies. *Philosophical Transactions of the Royal Society of London*, 115:513–583, 1825. doi: 10.1098/rstl.1825.0026.

H. J. Hagenaar and R. A. Shine. Moving magnetic features around sunspots. *The Astrophysical Journal*, 635:659–669, 2005. doi: 10.1086/497367.

K. Harvey and J. Harvey. Observations of moving magnetic features near sunspots. *Solar Physics*, 28:61–71, 1973. doi: 10.1007/BF00152912.

K. L. Harvey and F. Recely. Polar coronal holes during cycles 22 and 23. *Solar Physics*, 211:31–52, 2002. doi: 10.1023/A:1022469023581.

K. L. Harvey and C. Zwaan. Properties and emergence patterns of bipolar active regions. *Solar Physics*, 148:85–118, 1993. doi: 10.1007/BF00675537.

D. H. Hathaway. The solar cycle. *Living Reviews in Solar Physics*, 12:4, 2015. doi: 10.1007/lrsp-2015-4.

D. H. Hathaway. Royal Greenwich Observatory and USAF/NOAA sunspot group records, 1874–present. `http://solarcyclescience.com/activeregions.html`, 2024. Accessed 2026-07-20.

R. Henwood, S. C. Chapman, and D. M. Willis. Increasing lifetime of recurrent sunspot groups within the Greenwich Photoheliographic Results. *Solar Physics*, 262:299–313, 2010. doi: 10.1007/s11207-009-9419-5. arXiv:0907.4274.

H. Hotta and H. Iijima. On rising magnetic flux tube and formation of sunspots in a deep domain. *Monthly Notices of the Royal Astronomical Society*, 494:2523–2537, 2020. doi: 10.1093/mnras/staa844. arXiv:2003.10583.

R. Howe. Solar interior rotation and its variation. *Living Reviews in Solar Physics*, 6:1, 2009. doi: 10.12942/lrsp-2009-1. arXiv:0902.2406.

E. L. Kaplan and Paul Meier. Nonparametric estimation from incomplete observations. *Journal of the American Statistical Association*, 53(282):457–481, 1958. doi: 10.1080/01621459.1958.10501452.

Kislovodsk Mountain Astronomical Station, Pulkovo Observatory. Sunspot catalog of the Kislovodsk Mountain Astronomical Station. `https://observethesun.com`, 2026. Accessed 2026-07-31 via the observethesun.com API.

M. Kubo, B. W. Lites, T. Shimizu, and K. Ichimoto. Magnetic flux loss and flux transport in a decaying active region. *The Astrophysical Journal*, 686:1447–1453, 2008. doi: 10.1086/592064. arXiv:0807.4340.

Mei-Ling Ting Lee and G. A. Whitmore. Threshold regression for survival analysis: modeling event times by a stochastic process reaching a boundary. *Statistical Science*, 21(4):501–513, 2006. doi: 10.1214/088342306000000330.

P. C. Liewer, I. González Hernández, J. R. Hall, C. Lindsey, and X. Lin. Testing the reliability of predictions of far-side active regions from helioseismology using STEREO far-side observations of solar activity. *Solar Physics*, 289:3617–3640, 2014. doi: 10.1007/s11207-014-0542-6.

P. C. Liewer, J. Qiu, and C. Lindsey. Comparison of helioseismic far-side active region detections with STEREO far-side EUV observations of solar activity. *Solar Physics*, 292:146, 2017. doi: 10.1007/s11207-017-1159-3.

C. Lindsey and D. C. Braun. Seismic images of the far side of the Sun. *Science*, 287:1799–1801, 2000. doi: 10.1126/science.287.5459.1799.

Y. E. Litvinenko and M. S. Wheatland. Modeling sunspot and starspot decay by turbulent erosion. *The Astrophysical Journal*, 800(2):130, 2015. doi: 10.1088/0004-637X/800/2/130. arXiv:1501.01699.

Y. E. Litvinenko and M. S. Wheatland. Sunspot and starspot lifetimes in a turbulent erosion model. *The Astrophysical Journal*, 834(2):108, 2017. doi: 10.3847/1538-4357/834/2/108. arXiv:1611.03920.

D. W. Longcope and B. T. Welsch. A model for the emergence of a twisted magnetic flux tube. *The Astrophysical Journal*, 545:1089–1100, 2000. doi: 10.1086/317846.

V. I. Makarov and K. R. Sivaraman. On the epochs of polarity reversals of the polar magnetic field of the sun during 1870–1982. *Bulletin of the Astronomical Society of India*, 14:163–167, 1986.

D. Martin-Belda and R. H. Cameron. Surface flux transport simulations: Effect of inflows toward active regions and random velocities on the evolution of the Sun's large-scale magnetic field. *Astronomy & Astrophysics*, 586:A73, 2016. doi: 10.1051/0004-6361/201527213. arXiv:1512.02541.

D. Martin-Belda and R. H. Cameron. Inflows towards active regions and the modulation of the solar cycle: A parameter study. *Astronomy & Astrophysics*, 597:A21, 2017. doi: 10.1051/0004-6361/201629061. arXiv:1609.01199.

V. Martínez Pillet, F. Moreno-Insertis, and M. Vázquez. The distribution of sunspot decay rates. *Astronomy & Astrophysics*, 274:521–533, 1993.

F. Meyer, H. U. Schmidt, N. O. Weiss, and P. R. Wilson. The growth and decay of sunspots. *Monthly Notices of the Royal Astronomical Society*, 169:35–57, 1974. doi: 10.1093/mnras/169.1.35.

F. Meyer, H. U. Schmidt, and N. O. Weiss. The stability of sunspots. *Monthly Notices of the Royal Astronomical Society*, 179:741–761, 1977. doi: 10.1093/mnras/179.4.741.

J. Muraközy. Lifetime of long-lived sunspot groups. *Universe*, 10:318, 2024. doi: 10.3390/universe10080318.

Yu. A. Nagovitsyn and A. A. Pevtsov. On the presence of two populations of sunspots. *The Astrophysical Journal*, 833(1):94, 2016. doi: 10.3847/1538-4357/833/1/94.

Yu. A. Nagovitsyn and A. A. Pevtsov. Bi-lognormal distribution of sunspot group areas. *The Astrophysical Journal*, 906:27, 2021. doi: 10.3847/1538-4357/abc82d.

Yu. A. Nagovitsyn, A. A. Osipova, and A. A. Pevtsov. Tilt angle and lifetime of sunspot groups. *Monthly Notices of the Royal Astronomical Society*, 501(2):2782–2789, 2021. doi: 10.1093/mnras/staa3848.

Kosuke Namekata, Hiroyuki Maehara, Yuta Notsu, Shin Toriumi, Hisashi Hayakawa, Kai Ikuta, Shota Notsu, Satoshi Honda, Daisaku Nogami, and Kazunari Shibata. Lifetimes and emergence/decay rates of star spots on solar-type stars estimated by Kepler data in comparison with those of sunspots. *The Astrophysical Journal*, 871:187, 2019. doi: 10.3847/1538-4357/aaf471.

N. J. Nelson, B. P. Brown, A. S. Brun, M. S. Miesch, and J. Toomre. Buoyant magnetic loops in a global dynamo simulation of a young Sun. *The Astrophysical Journal Letters*, 739:L38, 2011. doi: 10.1088/2041-8205/739/2/L38. arXiv:1108.4697.

N. J. Nelson, B. P. Brown, A. S. Brun, M. S. Miesch, and J. Toomre. Buoyant magnetic loops generated by global convective dynamo action. *Solar Physics*, 289:441–458, 2014. doi: 10.1007/s11207-012-0221-4. arXiv:1212.5612.

H. W. Newton and M. L. Nunn. The Sun's rotation derived from sunspots 1934–1944 and additional results. *Monthly Notices of the Royal Astronomical Society*, 111(4):413–421, 1951. doi: 10.1093/mnras/111.4.413.

A. A. Norton, P. Charbonneau, and D. Passos. Hemispheric coupling: Comparing dynamo simulations and observations. *Space Science Reviews*, 186:251–283, 2014. doi: 10.1007/s11214-014-0100-4. arXiv:1411.7052.

E. N. Parker. Sunspots and the physics of magnetic flux tubes. I. The general nature of the sunspot. *The Astrophysical Journal*, 230:905, 1979. doi: 10.1086/157150.

B. Perri, H. Legrand, A. S. Brun, A. Finley, and A. Strugarek. Far-side active region emergence catalogue from Solar Orbiter/PHI. EGU General Assembly abstract EGU26-7581, 2026. doi: 10.5194/egusphere-egu26-7581.

K. Petrovay and F. Moreno-Insertis. Turbulent erosion of magnetic flux tubes. *The Astrophysical Journal*, 485:398–408, 1997. doi: 10.1086/304404.

K. Petrovay and L. van Driel-Gesztelyi. Making sense of sunspot decay. I. Parabolic decay law and Gnevyshev–Waldmeier relation. *Solar Physics*, 176:249–266, 1997. doi: 10.1023/A:1004988123265. arXiv:astro-ph/9706029.

K. Petrovay, V. Martínez Pillet, and L. van Driel-Gesztelyi. Making sense of sunspot decay. II. Deviations from the mean law and plage effects. *Solar Physics*, 188:315–330, 1999. doi: 10.1023/A:1005213212336. arXiv:astro-ph/9906258.

A. A. Pevtsov, V. M. Maleev, and D. W. Longcope. Helicity evolution in emerging active regions. *The Astrophysical Journal*, 593:1217–1225, 2003. doi: 10.1086/376733.

M. I. Pishkalo. On polar magnetic field reversal in solar cycles 21, 22, 23, and 24. *Solar Physics*, 294:137, 2019. doi: 10.1007/s11207-019-1520-9. arXiv:1909.00055.

M. Rempel. Subsurface magnetic field and flow structure of simulated sunspots. *The Astrophysical Journal*, 740:15, 2011. doi: 10.1088/0004-637X/740/1/15. arXiv:1106.6287.

M. Rempel and M. C. M. Cheung. Numerical simulations of active region scale flux emergence: From spot formation to decay. *The Astrophysical Journal*, 785:90, 2014. doi: 10.1088/0004-637X/785/2/90. arXiv:1402.4703.

D. Ruždjak, V. Ruždjak, R. Brajša, and H. Wöhl. Deceleration of the rotational velocities of sunspot groups during their evolution. *Solar Physics*, 221:225–236, 2004. doi: 10.1023/B:SOLA.0000035066.96031.4f.

P. H. Scherrer, J. M. Wilcox, L. Svalgaard, T. L. Duvall, P. H. Dittmer, and E. K. Gustafson. The mean magnetic field of the Sun: Observations at Stanford. *Solar Physics*, 54:353–361, 1977. doi: 10.1007/BF00159925.

M. Schüssler and M. Rempel. The dynamical disconnection of sunspots from their magnetic roots. *Astronomy & Astrophysics*, 441:337–346, 2005. doi: 10.1051/0004-6361:20052962. arXiv:astro-ph/0506654.

SILSO World Data Center. The international sunspot number, 13-month smoothed monthly total, version 2. `https://www.sidc.be/SILSO/`, 2026. Royal Observatory of Belgium, Brussels; series accessed 2026-07-31 via SILSO/INFO/snmstotcsv.php; dataset doi: 10.24414/qnza-ac80.

G. W. Simon and R. B. Leighton. Velocity fields in the solar atmosphere. III. large-scale motions, the chromospheric network, and magnetic fields. *The Astrophysical Journal*, 140:1120–1147, 1964.

S. K. Solanki. Sunspots: An overview. *Astronomy and Astrophysics Review*, 11:153–286, 2003. doi: 10.1007/s00159-003-0018-4.

D. R. Steinsaltz and K. W. Wachter. Understanding mortality rate deceleration and heterogeneity. *Mathematical Population Studies*, 13(1):19–37, 2006. doi: 10.1080/08898480500452117.

Bernard L. Strehler and Albert S. Mildvan. General theory of mortality and aging. *Science*, 132 (3418):14–21, 1960. doi: 10.1126/science.132.3418.14.

M. Švanda, M. Klvaňa, and M. Sobotka. Large-scale horizontal flows in the solar photosphere. V. Possible evidence for the disconnection of bipolar sunspot groups from their magnetic roots. *Astronomy & Astrophysics*, 506:875–884, 2009. doi: 10.1051/0004-6361/200912422. arXiv:0908.3183.

A. G. Tlatov, V. V. Vasil'eva, V. V. Makarova, and P. A. Otkidychev. Applying an automatic image-processing method to synoptic observations. *Solar Physics*, 289:1403–1412, 2014. doi: 10.1007/s11207-013-0404-7.

B. W. Turnbull. The empirical distribution function with arbitrarily grouped, censored and truncated data. *Journal of the Royal Statistical Society, Series B*, 38(3):290–295, 1976. doi: 10.1111/j.2517-6161.1976.tb01597.x.

L. van Driel-Gesztelyi and L. M. Green. Evolution of active regions. *Living Reviews in Solar Physics*, 12:1, 2015. doi: 10.1007/lrsp-2015-1.

J. W. Vaupel, K. G. Manton, and E. Stallard. The impact of heterogeneity in individual frailty on the dynamics of mortality. *Demography*, 16(3):439–454, 1979. doi: 10.2307/2061224.

J. W. Vaupel, J. R. Carey, K. Christensen, T. E. Johnson, A. I. Yashin, N. V. Holm, I. A. Iachine, V. Kannisto, A. A. Khazaeli, P. Liedo, V. D. Longo, Y. Zeng, K. G. Manton, and J. W. Curtsinger. Biodemographic trajectories of longevity. *Science*, 280(5365):855–860, 1998. doi: 10.1126/science.280.5365.855.

M. Waldmeier. *Ergebnisse und Probleme der Sonnenforschung*. Geest & Portig, Leipzig, 2nd edition, 1955.

D. F. Webb, J. M. Davis, and P. S. McIntosh. Observations of the reappearance of polar coronal holes and the reversal of the polar magnetic field. *Solar Physics*, 92:109–132, 1984. doi: 10.1007/BF00157239.

Waloddi Weibull. A statistical distribution function of wide applicability. *Journal of Applied Mechanics*, 18(3):293–297, 1951. doi: 10.1115/1.4010337.

Wilcox Solar Observatory. WSO polar magnetic field observations, 1976–present. `http://wso.stanford.edu/Polar.html`, 2026. Accessed 2026-07-31.

E. Wrigley-Field. Mortality deceleration and mortality selection: three unexpected implications of a simple model. *Demography*, 51(1):51–71, 2014. doi: 10.1007/s13524-013-0256-7.